

**STRUCTURAL AND METABOLIC MECHANISMS UNDERLYING THE  
BIOLOGICAL FATES OF TWO RESOURCE RECOVERY BIOPOLYMERS:  
POLYPHOSPHATE AND POLY(B-HYDROXYBUTYRATE)**

A Thesis Presented to the Faculty of the Graduate School of Cornell University  
In Partial Fulfillment of the Requirements for the Degree of Master of Science

by

Yeon soo Park

August 2021

© 2021 Yeon soo Park

## ABSTRACT

Resource recovery is an important aspect of environmental engineering for sustainability purposes, and polyphosphate (polyP) and poly( $\beta$ -hydroxybutyrate) (PHB) are examples of biopolymers that are utilized for resource recovery.

Given its structure composed of multiple phosphate groups linked by phosphoanhydride bonds, polyP is an important source of phosphorus (P) recovery from wastewaters. Polyphosphate accumulating organisms (PAOs) are an example of such a group of organisms since they are capable of storing P in the form of polyP when subjected to varying oxygen availability conditions. These organisms have been studied extensively to optimize the performance of enhanced biological P removal (EBPR) systems for wastewaters and previous studies have suggested the correlation between metal composition and EBPR performances. However, the underlying mechanism remains largely unknown. Therefore, in Chapter 1, we investigated the coordination of physiological metal cation ( $K^+$ ,  $Na^+$ ,  $Ca^{2+}$ , and  $Mg^{2+}$ ) chelated by polyPs of different chain lengths (with 10 and 30 phosphate moieties) by employing molecular dynamics simulations and experimental techniques. The simulation results showed that the Mg-polyP and K-polyP complexes were the most and least thermodynamically stable, respectively. Additionally, to gain insight into the conformation of polyP-30, we conducted gel permeation chromatography and small-angle X-ray scattering analysis on Mg-polyP-30 solution samples. Results showed varying thermodynamic stability amongst the tested metal-polyP complexes and we proposed the differing roles of metal-polyP complexes in maintaining the physiological pool of bacterial polyP: while the more thermodynamically stable Mg-polyP complexes could contribute to the long-term storage of polyP, the less stable K-polyP with weaker chelating strength would allow and favor enzymatic hydrolysis of polyP.

Chapter 2 focuses on PHB which, due to its similar physical properties to conventional, petroleum-based plastics, is an attractive source of bioplastic. Accumulation of PHB in various

organisms under nutrient limitations has been well reported, and *Comamonas testosteroni* is also capable of accumulating PHB under nutrient deficiency. However, how nutrient limitation induces PHB accumulation in bacteria like *C. testosteroni* remains unclear. Therefore, to gain insight into the nutrient-dependent carbon metabolism that leads to PHB production by *C. testosteroni*, we first investigated the effect of varying nutrient conditions on biomass growth of *C. testosteroni* KF-1. Second, we employed a quantitative  $^{13}\text{C}$ -metabolic flux analysis (MFA) using ultra-high-performance liquid chromatography with high-resolution mass spectroscopy to understand the effect of nitrogen (N) availability on carbon metabolism. Third, we compared the metabolite levels and relative protein abundances for the different N and P conditions to gain insight into how reduced nutrient availability may have impacted the cell's response. Our findings implied that *C. testosteroni* is less sensitive to P-deficiency than to N-deficiency and that there may be a threshold at which N depletion favors the production of PHB compared to the replete condition due to compromised cellular growth further imposing imbalances between the metabolic carbon flux and energetics.

## **BIOGRAPHICAL SKETCH**

Yeonsoo Park earned her Bachelor of Science degree from Cornell University. She graduated in May 2019 with honors in Environmental Engineering and a minor in Applied Mathematics. In Fall 2019, she joined the Biological and Environmental Engineering graduate program at Cornell University. Yeonsoo's thesis research was supervised by Drs. Ludmilla Aristilde and April Z. Gu who also served on her thesis committee.

## ACKNOWLEDGMENTS

I am sincerely grateful to my advisors, Drs. Ludmilla Aristilde and April. Gu, for their mentorship, guidance, and encouragements over the past two years. I deeply appreciate the unique experience that I had by joining and doing research in both labs. I thank Dr. Christos Malliakas for his guidance and assistance in applying X-ray scattering techniques and analyzing the results. I would also like to thank Dr. Jacob Waldbauer for this assistance in preparing and analyzing proteomics data. I truly appreciate my colleagues from April Z. Gu group for welcoming me to the lab, introducing bacterial and engineering research techniques, and all the help that they supplied. I would also like to thank my fellow colleagues from Aristilde research group for the time spent together troubleshooting the machines, all of our discussions whenever my research faced an obstacle, and the tremendous support that they supplied. I also give my special thank you to Rebecca Wilkes, my mentor who taught me the experimental techniques, gave me great advice, and troubleshoot the MFA with me.

## TABLE OF CONTENTS

ABSTRACT.....	i
BIOGRAPHICAL SKETCH .....	iii
ACKNOWLEDGMENTS .....	iv
LIST OF FIGURES .....	vii
LIST OF TABLES .....	viii

### **CHAPTER 1: Molecular coordination, structure, and stability of metal-polyphosphate complexes resolved by molecular modeling and x-ray scattering: structural insights on the biological fate of polyphosphate**

1. Introduction.....	9
2. Materials and Methods.....	11
2.1 Computational modeling of metal-polyP complexes.....	11
2.2 Experimental analysis of metal-polyP complexes .....	14
3. Results and Discussion .....	17
3.1 Relative thermodynamic stability predicted by molecular simulations of metal-polyP complexes .....	17
3.2 Molecular modeling of metal coordination in the metal-poly-P complexes.....	19
3.3 Experimental corroboration of Mg-polyP-30 conformation and coordination using GPC, TXS, and SAXS .....	23
3.4 Implications for the biological and environmental fates of metal-polyP complexes.....	25

### **CHAPTER 2: Multiomics analysis of nutrient-dependent growth and biosynthetic demand for poly( $\beta$ -hydroxybutyrate) in *Comamonas testosteroni* KF-1**

1. Introduction.....	29
2. Materials and Methods.....	31
2.1 Materials. ....	31

2.2	Culturing conditions and growth measurements.....	31
2.3	Acetate consumption and extracellular nutrient measurements.....	33
2.4	Metabolite Quantification.....	33
2.5	Intracellular PHB measurements.....	35
2.6	Quantitative MFA and cofactor balance for the N limited condition.....	36
2.7	Proteomics.....	36
2.8	Metabolite level and relative protein abundance visualization.....	37
3.	Results and Discussion.....	38
3.1	Growth response of <i>C. testosteroni</i> KF-1 to nutritional availability of N and P.....	38
3.2	Changes in metabolic pathways and fluxes in response to N limitation.....	41
3.3	Nitrogen metabolism.....	46
3.4	Nutrient dependent metabolome and proteome changes.....	47
4.	Conclusion.....	49
	REFERENCES.....	51
	APPENDIX A: Chapter 1.....	59
	APPENDIX B: Chapter 2.....	63

## LIST OF FIGURES

**Figure 1.1** Molecular dynamics snapshot of optimized hydrated Ca-polyP complexes and the percent difference of total potential energies of the metal-polyP complexes

**Figure 1.2** Radial distribution functions of different O groups within metal-polyP complexes

**Figure 1.3** Molecular dynamics snapshots of each metal-polyP complex

**Figure 1.4** Comparison of Mg-polyP-30 complex size distribution with different methods

**Figure 1.5** Comparison of experimental and computational data of the coordination environment in the Mg-polyP-30 complex

**Figure 2.1** Growth rates of *C. testosteroni* KF-1 grown on varying C, N, and P availabilities

**Figure 2.2** Schematic of carbon metabolism in *C. testosteroni* KF-1

**Figure 2.3** Cofactor balances in *C. testosteroni* KF-1

**Figure 2.4** Schematic of ammonium assimilation

**Figure 2.5** Poly( $\beta$ -hydroxybutyrate) levels, metabolome, and proteome profiling of different nutrient conditions

## LIST OF TABLES

**Table 1.1** Coordination distance, number, and geometry of each metal-polyP complexes

**Table 2.1** Elemental composition of *C. testosteroni* biomass

## CHAPTER 1

# MOLECULAR COORDINATION, STRUCTURE, AND STABILITY OF METAL-POLYPHOSPHATE COMPLEXES RESOLVED BY MOLECULAR MODELING AND X-RAY SCATTERING: STRUCTURAL INSIGHTS ON THE BIOLOGICAL FATE OF POLYPHOSPHATE

Yeonsoo Park<sup>1,2</sup>, Christos D. Malliakas<sup>3</sup>, Qing Zhou<sup>4,5</sup>, April Z. Gu<sup>4</sup>, Ludmilla Aristilde<sup>1,2</sup>

<sup>1</sup> Department of Biological and Environmental Engineering, College of Agriculture and Life Sciences, Cornell University, Ithaca, NY 14853 USA

<sup>2</sup> Department of Civil and Environmental Engineering, McCormick School of Engineering and Applied Science, Northwestern University, Evanston, IL 60208 USA

<sup>3</sup> Department of Chemistry, Northwestern University, Evanston, IL 60208 USA

<sup>4</sup> Department of Civil and Environmental Engineering, College of Engineering, Cornell University, Ithaca, NY 14853 USA

<sup>5</sup> School of the Environment, Nanjing University, Nanjing, Jiangsu Province 210023, China

### 1. Introduction

Polyphosphate (polyP), a polymer of two or more phosphate moieties synthesized by all living organisms, has various biological functions including serving as a phosphorus (P) reservoir, supporting energy supply as a phosphoryl donor for adenylate kinase, acting as a strong metal chelator in bacteria, and buffering the effects of environmental stresses such as nutrient deficiencies, heat, and extreme pH.<sup>1-4</sup> Of particular interest are the polyP-accumulating organisms (PAOs), which are bacteria capable of storing P up to four to ten times greater than the normal cellular levels in the form of polyP.<sup>5,6</sup> These organisms have been studied most extensively within the context of engineered systems, namely enhanced biological P removal (EBPR) systems for wastewater treatment.<sup>3,4</sup> In addition to engineered systems, the importance

of PAOs and polyPs has recently been highlighted in natural environments such as terrestrial, freshwater, and marine.<sup>3,4</sup> Notably, given their phenotypic and genetic diversity, PAOs have been considered to play a critical role in both engineered and natural P cycling through the synthesis, storage, and utilization of polyPs.<sup>3,4</sup> To gain insights into the importance of different metal complexes with polyP in the biological fate of polyP, a molecular investigation of the structure, coordination, and stability of these complexes is warranted.

As a polyelectrolyte, polyP is amenable to complexing the metal cations that serve as counterions to the negatively charged phosphate moieties. In fact, metal composition and metal-polyP complexes have been implicated to play an important role in EBPR performance.<sup>3,7-14</sup> Using combined microscopic and spectroscopic analyses, a recent study of metal-polyP composition in different EBPR systems revealed the selective localization of Mg and K over Na and Ca in polyP granules in PAO cells, as well as the varying metal-specific metal ion to P stoichiometric ratios.<sup>15</sup> Furthermore, correlation analysis implied that the Mg-polyP content was especially important for promoting the stability of EBPR operations.<sup>15</sup> Metal cations in soils and waters are also expected to dictate the behavior of polyPs and PAOs in natural environmental matrices. However, mechanistic information on metal complexation by bacterial polyPs is not well known.

Bacterial polyP chains, which can vary in lengths, can contain up to thousands of phosphate moieties.<sup>2,16</sup> There are numerous studies on the coordination of metal complexes with pyrophosphate, the shortest polyP molecule (see review by Ikotun *et al.*<sup>16</sup> and references therein) and phosphate glasses (see review by Sharmin and Rudd<sup>17</sup> and references therein). Beyond the discrepancy between the short-chain pyrophosphate and reported chain lengths for bacterial polyP, whether structural information on the crystalline phosphate glasses is relevant to

physiological metal-polyP complexation conditions requires further investigation. Particularly relevant to understanding and predicting the biological fate of polyP with respect to the formation of metal-polyP complexes, it is important to obtain structural insights on these complexes with physiologically relevant metal cations.

To this end, we sought to elucidate the molecular coordination, structure, and stability of polyP complexes with  $\text{Na}^+$ ,  $\text{K}^+$ ,  $\text{Ca}^{2+}$ , and  $\text{Mg}^{2+}$ . We employed a combination of molecular modeling simulations and experimental measurements. Firstly, we performed annealing Monte Carlo simulations coupled with molecular dynamics equilibration to obtain thermodynamically optimized structures of the fully hydrated metal-polyP complexes with explicit water molecules. The model structures were used to predict the coordination geometry and stability of metal complexes with polyP chains of different lengths, with 10 and 30 phosphate moieties (thereafter, named polyP-10 and polyP-30). Secondly, to obtain corroborating experimental evidence of the predicted structures, we performed gel permeation chromatography (GPC), total X-ray scattering (TXS) analysis, and small-angle X-ray scattering (SAXS) of a prepared Mg-polyP-30 solution. We interpret our results in terms of the relationship between stability and favorable geometry of metal complexation by polyP. Our study appears to be the first to obtain structural insights on metal-polyP complexes, a fundamental knowledge that is required to achieve a mechanistic understanding of the biological fate of polyP in PAOs in both natural and engineered systems.

## **2. Materials and Methods**

**2.1 Computational modeling of metal-polyP complexes.** *2.1.1 Modeling platform.* The Chemistry at HARvard Macromolecular Mechanics (CHARMM) forcefield as implemented within the Discovery Studio software package (Biovia) was employed to obtain the speciation (at

pH 7) of each polyP molecule (polyP-10 and polyP-30) in a solvated environment. Subsequent simulations of the solvated metal-polyP complexes were conducted using the all-atom condensed-phase optimized molecular potentials for atomistic simulation studies (COMPASS, version II) force-field and the Forcite module within the Materials Studio software package.<sup>18</sup> All the partial charges and interatomic parameters were in accordance with the COMPASS II forcefield, except that those for the water molecules were assigned SPC/E charges.

*2.1.2 Validation of modeling platforms and forcefield applications.* No structural data were available for longer chains of polyP. Therefore, we conducted validation simulations with a Ca-pyrophosphate complex, for which there were published X-ray structural data, to validate that the COMPASS II forcefield was adequate for simulating metal-polyP in our systems.

Acknowledging that our targeted polyP chains are longer than the pyrophosphate, the goal of our validation simulations was to evaluate the ability of our protocol to achieve optimized structural configurations of the phosphoanhydride (i.e., phosphate-phosphate) bond as well as the coordination geometry of metal complexation by phosphate ligands. The Ca-pyrophosphate complex was initially prepared at pH 4.5 as done in the published study<sup>19</sup> and solvated with explicit water molecules (with a minimum of 5 Å-thick water layer) using the Discovery Studio platform with the CHARMM forcefield. The prepared complex was subjected to a series of simulations consisting of energy minimization and annealing molecular dynamics (five cycles from 363 to 600 K) as previously described.<sup>20,21</sup> Structural data were retrieved from a 10-ns molecular dynamics equilibration run (time step = 1 fs), wherein the potential energy profile was equilibrated after less than 0.5 ns. The molecular dynamics run was carried out in a canonical NVT ensemble (fixed number of atoms, simulation cell volume, and constant temperature) using a canonical Berendsen thermostat to maintain the temperature at 363 K as done in the published

study.<sup>19</sup> Compared to the experimental structural data, the optimized configuration of the simulated Ca-pyrophosphate yielded less than 6% and 12% difference (on average) from the measured values of 10 bond lengths and 13 bond angles, respectively (Table S1.1).<sup>19</sup>

*2.1.3 Simulations of metal-polyP complexes.* Following the validated procedure described above, polyP-10 and polyP-30 were both prepared at pH 7 and solvated with explicit water molecules. Subsequently, the solvated polyP molecules were imported into the Materials Studio platform to obtain the energy-optimized structures using the COMPASSII forcefield, as described above. To obtain each metal-polyP complex, the Adsorption Locator module was used to subject each metal cation ( $\text{Na}^+$ ,  $\text{K}^+$ ,  $\text{Ca}^{2+}$ , or  $\text{Mg}^{2+}$ ) to translation and rotation steps with respect to the (dry) poly-P molecule during an annealing Monte Carlo search with a temperature cycle from 298 K to 600 K, repeated five times, followed by a preliminary 1-ns molecular dynamics equilibration of the resulting metal-polyP complex at 298 K. Subsequently, the solvation sphere of water molecules (from the aforementioned solvation procedure) was allowed to assume an optimal solvation arrangement around the metal-polyP complex using the Adsorption Locator module. The final solvated metal-polyP system was subjected to a final molecular dynamics equilibration run for 10 ns. In all eight hydrated metal-polyP complexes (four different metal complexes for the two polyP chains), equilibrium of the potential energy profiles occurred in less than 0.5 ns.

*2.1.4 Molecular Modeling Analysis.* All configurations obtained from the final 10-ns molecular dynamics run were used to retrieve thermodynamic and structural data. We computed the statistics for the total potential energy, and interatomic distance between the metal cations and different O atoms in the system. Total potential energies for the metal-polyP complexes were used to evaluate their relative thermodynamic stability.<sup>20,21</sup> The three O atoms analyzed for the

metal coordination were: O atoms in water molecules (water O), the deprotonated O atoms of the polyP molecule (ligand O), and the O atoms in the phosphoanhydride bond within the polyP molecule (bridging O). We employed the Forcite module in Materials Studio to obtain radial distribution functions (RDFs) for the metal-O atom pairs using a bin interval of 0.06 Å. The coordination numbers (CNs) were calculated by first integrating the RDF up to the first global minimum. To obtain the most likely coordination geometry of each complex, the CN numbers were recalculated up to the radial distance at which the CN value was close to the rounded-up whole number of the previously obtained CN for each case (Table S1.2; Figure S1.1). The coordination geometry of each complex was determined by gathering the possible geometries based on the sum of coordination numbers (CNs) and then assigning the specific geometry by comparing the CN of each O group within the range of the coordination distance from the metal cation. For each metal-O pairs, we conducted a one-way analysis of variance (ANOVA) test on the coordination distances reported in Table 1.1 followed by a post-hoc Tukey-Kramer test to discern the metals that have statistically significant differences in the coordination distances.

**2.2 Experimental analysis of metal-polyP complexes.** To obtain experimental corroboration, we conducted GPC and X-ray scattering measurements on a solution of Mg-complexed polyP-30.

*2.2.1 Synthesis of polyP-30 and preparation of Mg-polyP-30.* A polyP-30 ( $P_{30}O_{91}Na_{32}$ ) was obtained using a previously published procedure<sup>22</sup> whereby hydrated sodium dihydrogen phosphate ( $NaH_2PO_4 \cdot H_2O$ ) was gradually heated to 700 °C, followed by the removal of oxide and hydroxide layers with acetic acid and NaCl and quenching on a copper plate. Subsequently, the polyP-30 glass was fractioned by grinding, dissolving in deionized water, stirring, and performing serial addition of acetone. Finally, the precipitate in the solution was collected,

frozen at  $-20\text{ }^{\circ}\text{C}$ , and then lyophilized. The degree of polymerization of the produced polyP was determined by  $^{31}\text{P}$ -NMR analysis. The Mg-polyP-30 solution was prepared by dissolving 52 mM of  $\text{MgCl}_2$  obtained from Sigma-Aldrich (St. Louis, MO) and 3.3 mM of the synthesized polyP-30; a reference solution containing only  $\text{MgCl}_2$  at the same concentration was also prepared. The concentrations were decided on to ensure Mg-polyP-30 complexation yet to prevent the precipitation of the Mg-polyP-30 complex. All solutions were prepared with the ultrapure water obtained with the Barnstead™ GenPure™ water purification system (Thermo Scientific, Waltham, MA).

*2.2.2 Small-angle X-ray scattering.* The SAXS measurements for the determination of the particle distribution were performed at the beamline 5ID-D of the Advanced Photon Source (APS) at the Argonne National Lab. A vacuum flow-cell setup was used at 10 KeV of photon energy. A triple detector system (hs102, hs103, and hs104) from Rayonix was used for diffraction intensity measurements. The position of the 2-dimensional detector was calculated by measuring silver behenate ( $\text{AgC}_{22}\text{H}_{43}\text{O}_2$ ) as a standard. Additionally, glassy carbon was used for the determination of the calibration factor for the SAXS data, and water scattering data from the medium angle scattering region were used for the determination of the thickness of the sample capillary. Measurements of the sample (Mg-polyP-30) solution and the reference solution ( $\text{MgCl}_2$ ) were obtained at a sample load speed of  $20\text{ }\mu\text{l/s}$ . An exposure of 10 s per frame was used for the total collection of 5 frames per sample. The reference solution was used as a baseline correction for the SAXS analysis. The vacuum flow cell was washed with flowing soap and water and rinsed with water between each measurement. The radius distribution of the Mg-polyP-30 complex using the SAXS data obtained at the beamline was determined using the Interior-Point Gradient method for fitting the experimental data. Data processing was performed

with the GSAS-II software package. From the SAXS data, multiple shape models were tested to obtain respective size distributions. Subsequently, the size distribution was compared to that obtained from the GPC analysis (described in a later section). The results were most comparable when a spherical model was assumed.

*2.2.3 Total scattering using Pair Distribution Function.* Total scattering data for the Mg-polyP-30 solution and the reference MgCl<sub>2</sub> solution were collected at room temperature at the Integrated Molecular Structure Education and Research Center (IMSERC) at Northwestern. Each liquid sample was loaded into a Kapton capillary (1.65 mm in diameter) and mounted on a STOE StadiVari diffractometer equipped with an AXO Ag K $\alpha$  micro-focus sealed X-ray source A-MiXS, running at 65 kV and 0.68 mA, and a Dectris Pilatus3 R CdTe 300K Hybrid Photon Counting detector. The data were integrated using the program GSAS-II and corrections (such as subtraction of the container and subsequent correction by the reference solution, Compton and fluorescence scattering, geometric and absorption corrections) were performed using the program PDFgetX3.<sup>23</sup> The normalized data were truncated at 20 Å<sup>-1</sup> before pair distribution function (PDF) calculation (details available in Supporting Information). For comparative analysis, given that the experimental PDF accounts for all atom-to-atom interactions within the sample, we also obtained the PDF for the Mg paired with all O atoms within the simulated Mg-polyP-30 system using a bin interval of 0.06 Å.

*2.2.4 Gel permeation chromatography analysis.* Aqueous GPC was performed using the prepared Mg-polyP-30 solution. Data were collected using the Astra Version 7 data acquisition software and processed using Astra Version 7. The instrument was configured with an Agilent 1260 Series high-performance liquid chromatography module equipped with an ultraviolet detector and coupled with Wyatt Heleos II Multi-Angle static Light Scattering and Refractive

Index detectors. The size-exclusion chromatographic analysis was run on a PSS Suprema column (diameter 7.6 mm x length 250 mm) at a flow rate of 1 mL/ min with phosphate-buffered saline as a mobile phase. The particle size was derived from the scattering theory developed by Ludvig Lorenz, which represents an exact solution of Maxwell's electromagnetic theory.<sup>24</sup> There were no restrictions on the particle's refractive index or size, and the ASTRA software was used to determine the radius of homogeneous spherical particles.

### **3. Results and Discussion**

**3.1 Relative thermodynamic stability predicted by molecular simulations of metal-polyP complexes.** Using the total potential energy from our molecular dynamics simulations, we evaluated the relative stability of the metal-polyP complex whereby the most stable complex would exhibit the lowest potential energy value (Figure 1.1C). Due to the reference algorithm for the energy parameters in the forcefield, these calculated energies can only be compared across metal complexes with the same polyP molecule.<sup>20</sup> The total potential energy for the complexes of polyP-10 with Na<sup>+</sup>, K<sup>+</sup>, Ca<sup>2+</sup>, and Mg<sup>2+</sup> was  $-22,600.7 \pm 143.4$ ,  $-22,111.4 \pm 72.3$ ,  $-24,044.1 \pm 115.8$ , and  $-24,191.4 \pm 62.5$  kcal/mol, respectively (Figure 1.1C). For the metal-polyP-30 complexes, the total potential energy was  $-76,471.7 \pm 265.2$ ,  $-73,911.7 \pm 332.6$ ,  $-81,154.6 \pm 247.7$ , and  $-82,752.8 \pm 180.4$  kcal/mol for Na<sup>+</sup>, K<sup>+</sup>, Ca<sup>2+</sup>, and Mg<sup>2+</sup>, respectively (Figure 1.1C).

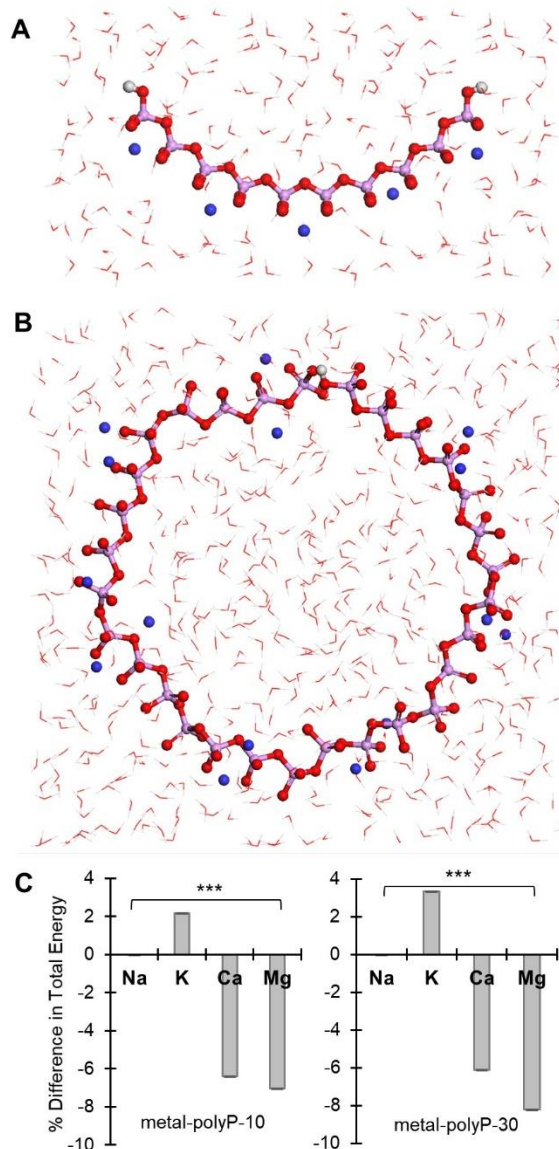


**Figure 1.1** (A) Snapshot of molecular-dynamics optimized hydrated Ca-polyP-10 complex. (B) Snapshot of molecular-dynamics optimized hydrated Ca-polyP-30 complex. (C) Percent (%) difference of the total potential energies of (A) metal-polyP-10 and (B) metal-polyP-30 respective to the corresponding Na-polyP. The asterisks (\*\*\*) mark that all cases had statistically significant differences with a  $p$ -value  $< 0.05$  when comparing the total potential energies of each cases.

Figure 1.1C illustrates the comparison of the percent difference of the total potential energy for each complex relative to the respective Na-polyP complex. Therefore, the stability order for both metal-polyP10 and metal-polyP30 complexes was  $Mg^{2+} > Ca^{2+} > Na^{+} > K^{+}$  (Figure 1.1C). The predicted stability order was consistent with the inverse order of the ionic potentials of the metal cations, as would be expected for electrostatic interactions.<sup>25</sup> In EBPR

systems, the presence of Na-, K-, Ca-, and Mg-polyP was evident in the polyP granules of PAOs.<sup>15</sup> Remarkably, only the Mg-polyP complex, which we determined was the most thermodynamically stable complex, was found to be preferred in intracellular polyP granules and its abundance was shown to correlate positively with EBPR performance.<sup>15</sup> We further analyzed our model metal-polyP structures to determine the role of the coordination geometry of the complexed metal, a structural insight that has not yet been elucidated for metal-polyP complexes.

**3.2 Molecular modeling of metal coordination in the metal-poly-P complexes.** From the RDFs of the thermodynamically optimized systems, we calculated both the coordination distance and the coordination number of each metal-O pair in the metal-polyP complexes (Figure 1.2; Table 1.1). For the metal complexation by polyP-10 ligand O, the ANOVA test on the coordination distances reported significant variation among the four metals [F(3,26)=7.002,  $p=0.001$ ] but further post-hoc Tukey-Kramer test showed that only Mg<sup>2+</sup> compared to K<sup>+</sup> or Na<sup>+</sup> had a statistically significant difference ( $p < 0.05$ ). For the metal complexation by polyP-10 bridging O, there was significant variation among the metals [F(3,26)=12.025,  $p < 0.001$ ] and all metals had statistically significant differences ( $p < 0.05$ ) except when Ca<sup>2+</sup> was compared to K<sup>+</sup> or Na<sup>+</sup>. Both statistical analyses implied that the coordination distances for Mg with polyP O atoms was significantly smaller than the other metals analyzed. For metal complexation by polyP-10 water O, there were no significant variation among the metals [F(3,26)=1.245,  $p=0.312$ ]. Therefore, it was implied that the differences in thermodynamic stability of metal-polyP complexes should be attributed to the complexation by the polyP ligand O and bridging O. Consistent with the reverse order of the thermodynamic stability order, the coordination distance for all metal-polyP-10 O atoms increased in the order from Mg<sup>2+</sup>, Ca<sup>2+</sup>, Na<sup>+</sup>, to K<sup>+</sup> (Table 1.1).

For metal-polyP-30 ligand O, there was significant variation among the metals [F(3,86)=9.929,  $p < 0.001$ ] and all comparisons had statistically significant differences ( $p < 0.05$ ) except when comparing  $\text{Ca}^{2+}$  to  $\text{Mg}^{2+}$  and  $\text{K}^+$  to  $\text{Na}^+$ . Therefore, the coordination distances of divalent metal cations to polyP-30 ligand O were significantly smaller than those of the monovalent metal cations. For the metal complexation by polyP-30 bridging O, again there was significant variation [F(3,86)=28.279,  $p < 0.001$ ] and all comparisons but that between  $\text{Ca}^{2+}$  and  $\text{K}^+$  had statistically significant differences ( $p < 0.05$ ). For the metal complexation by polyP-30 water O, there was significant variation [F(3,86)=5.094,  $p=0.003$ ] and only the comparisons of  $\text{Ca}^{2+}$  with  $\text{K}^+$  and  $\text{Na}^+$  were statistically significantly different ( $p < 0.05$ ). The coordination distances for metal-polyP-30 ligand O and water O increased in an order similar to that for metal-polyP-10 and O pairs ( $\text{Mg}^{2+} = \text{Ca}^{2+} < \text{Na}^+ = \text{K}^+$ ) (Table 1.1). However, for metal-polyP-30 bridging O, the coordination distance increased from  $\text{Mg}^{2+}$ ,  $\text{Na}^+$ ,  $\text{K}^+$ , to  $\text{Ca}^{2+}$  (Table 1.1) Therefore, for polyP-30, the order of coordination distances for the metal complexation by polyP ligand O followed the thermodynamic stability trend, implying that the thermodynamic stability of the metal-polyP complexes was in accordance with the strength of metal chelation by the polyP ligand O.

**Table 1.1** Coordination distance (average  $\pm$  standard deviation, Å), coordination number (CN), and coordination geometry of the metal (M)-polyphosphate (polyP) complexes

M (metal)	M-ligand O		M-bridging O		M-water O		Coordination Geometry
	Distance	CN	Distance	CN	Distance	CN	
<i>M-polyP-10 complexes</i>							
$\text{Na}^+$	2.37 $\pm$ 0.44	1.50	2.16 $\pm$ 0.22	0.40	2.40 $\pm$ 0.82	2.44	Square pyramid
$\text{K}^+$	2.70 $\pm$ 0.46	1.99	2.52 $\pm$ 0.29	0.40	2.52 $\pm$ 0.22	1.20	Square pyramid
$\text{Ca}^{2+}$	2.28 $\pm$ 0.29	1.80	2.16 $\pm$ 0.22	1.20	2.19 $\pm$ 0.71	0.40	Trigonal pyramid
$\text{Mg}^{2+}$	1.71 $\pm$ 0.16	1.82	1.74 $\pm$ 0.18	1.40	1.95 $\pm$ 0.09	0.20	Square pyramid
<i>M-polyP-30 complexes</i>							
$\text{Na}^+$	2.61 $\pm$ 0.58	2.59	2.19 $\pm$ 0.27	0.20	2.49 $\pm$ 0.37	2.04	Trigonal biprism
$\text{K}^+$	2.64 $\pm$ 0.42	1.83	2.43 $\pm$ 0.13	0.03	2.55 $\pm$ 0.27	1.44	Trigonal bipyramid
$\text{Ca}^{2+}$	2.16 $\pm$ 0.25	1.36	2.49 $\pm$ 0.23	0.33	2.19 $\pm$ 0.16	0.77	Trigonal pyramid
$\text{Mg}^{2+}$	2.01 $\pm$ 0.34	2.36	1.89 $\pm$ 0.20	0.13	2.34 $\pm$ 0.39	1.60	Square pyramid

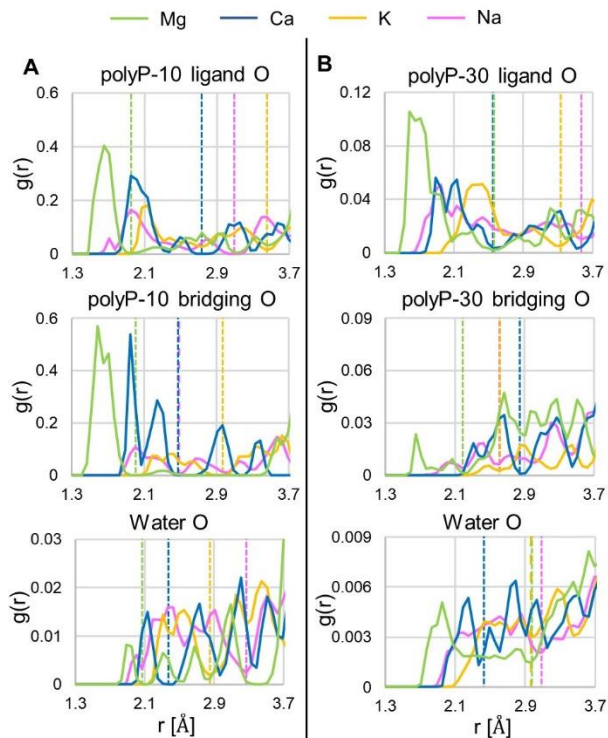


**Figure 1.2** Radial distribution functions (RDF,  $g(r)$ ) of different O groups within the metal (M)-polyphosphate (polyP) complexes: (A) polyP-10 and (B) polyP-30. The dotted lines mark the radial distance at which the global minimum was detected and used for coordination number (CN) calculations. Color code: Na (pink), K (yellow), Ca (blue), and Mg (green).

The CN values of the polyP ligand O (1.5 – 2.6) were greater than those of the bridging O (0.1 – 1.4) in all cases by  $52.4 \pm 28.4$  % for metal-polyP-10 complexes and by  $90.2 \pm 10.0$  % for metal-polyP-30 complexes (Table 1.1), indicating a greater contribution of the ligand O than the bridging O in the metal complexation by polyP. The CN values for water O varied among the metal-polyP complexes, ranging from 0.2 to 2.4 (Table 1.1) – the CN values of the water O in metal-polyP-30 complexes was not well determined due to the lack of a clear global minimum for the CN calculation (Figure 1.2).

For determining the metal coordination geometries, we used rounded values of the CN values reported in Table 1.1 (Table S1.2). We found that, the specific coordination geometry was well conserved for divalent metal complexes for both polyP chain lengths: a trigonal pyramid

coordination geometry for the Ca-polyP complexes, and a square pyramid coordination geometry for the Mg-polyP complexes (Figure 1.3; Table 1.1). However, for the monovalent metal complexes, the coordination geometries were not conserved for different polyP chain lengths. The Na-polyP complexes had a square pyramid and trigonal bipyramid coordination geometries for polyP-10 and polyP-30, respectively. While the K-polyP-10 complex also had a square pyramid coordination geometry, the K-polyP-30 complex had a trigonal bipyramid coordination geometry. In all metal complexes except the  $Mg^{2+}$  complexes, there were minor distortions from the regular polyhedron coordination geometries (Figure 1.3), which may be attributed to Jahn-Teller geometrical distortions of non-linear molecules towards obtaining a thermodynamically optimized stable configuration.<sup>26,27</sup>

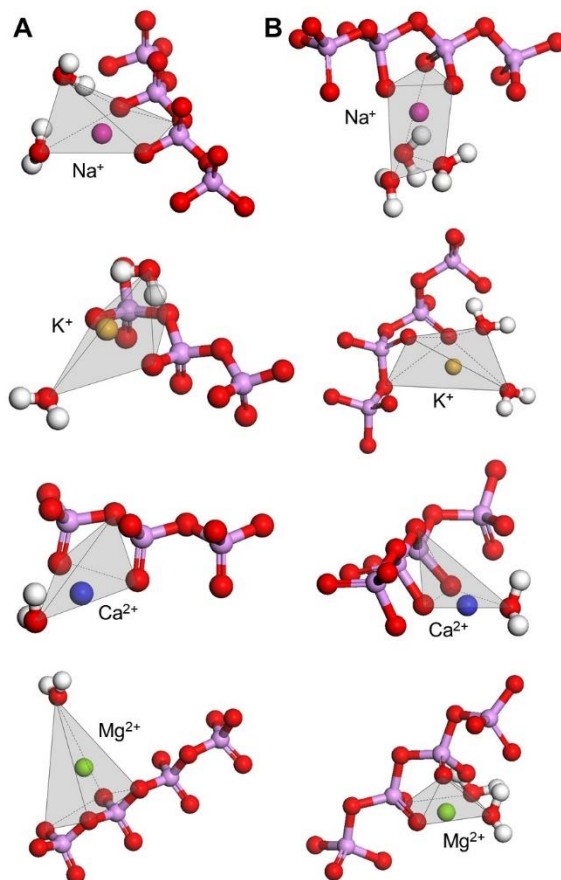


**Figure 1.3** Close-ups of molecular dynamics snapshots for each metal complex with (A) polyP-10 or (B) polyP-30. From top to bottom, Na<sup>+</sup> (pink), K<sup>+</sup> (yellow), Ca<sup>2+</sup> (blue), and Mg<sup>2+</sup> (green). For each complex, solvated waters not involved in the coordination of the metal was removed and adjacent Pi moieties of the polyP backbone was included on each side of the coordinated O within the molecule for clarity.

**3.3 Experimental corroboration of Mg-polyP-30 conformation and coordination using GPC, TXS, and SAXS.** Polyphosphate has been considered to assume three different conformations: open linear chains, closed rings, and caged structures with branched phosphate groups.<sup>28</sup> The molecular dynamics-optimized structures predicted a curved linear configuration for the metal-polyP-10 complexes, but the metal-polyP-30 complexes had a ring-like conformation (albeit not a closed circle), as illustrated in Figures 1.1A and B for Mg-polyP-10 and Mg-polyP-30, respectively. These results implied a polyP chain length threshold that would determine transition from linear to circular configurations. Determining this threshold was beyond the scope of our data.

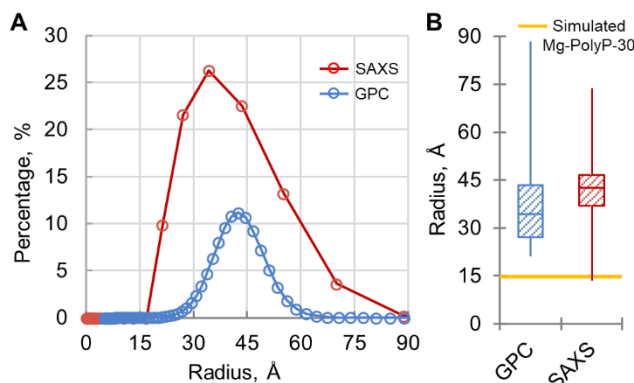


**Figure 1.4** Comparison of the size distribution results for Mg-polyphosphate (polyP)-30 complexes analyzed with different methods: (A) size distribution of the circular polyP-30 molecule's radius obtained from gel permeation chromatography (GPC) (blue) and small angle X-ray scattering (SAXS) (red). (B) Box plots of the results from GPC and SAXS overlapped with a line marking the radius obtained from the MD simulation model (yellow). Each box plot was created by taking the 1<sup>st</sup>, 2<sup>nd</sup>, and 3<sup>rd</sup> quartile of the data and the lines mark the range of the experimentally measured radius.

We conducted both GPC and SAXS analyses to probe experimentally the occurrence of the circular Mg-polyP-30 complexes in solution. The radius ranged from 21.3 to 88.7 Å for Mg-polyP-30 calculated from the GPC data and ranged from 13.5 to 74.0 Å from the SAXS analysis (Figure 1.4A). The radius ( $14.8 \pm 0.0$  Å) of the circular conformation of the simulated Mg-

polyP-30 was within two standard deviations of the averaged radius values obtained with the GPC analysis and at the low end of the radius range obtained with the SAXS analysis (Figure 1.4B). Therefore, the experimental analysis highlighted the simultaneous presence of both curved linear chain and circular ring conformations of the Mg-polyP-30 complex, but a circular conformation was revealed to be thermodynamically favorable for the simulated polyP-30 complex (Figure 1.1 and 1.4).

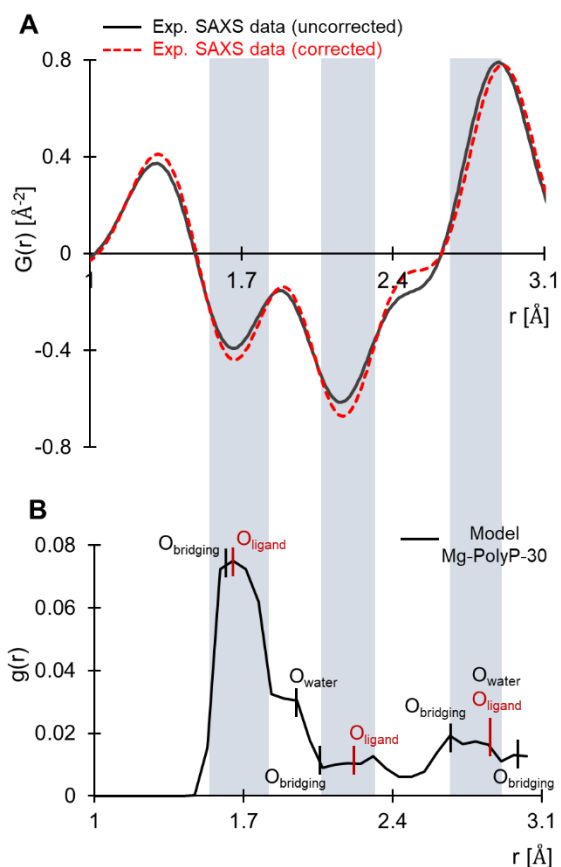


**Figure 1.5** Comparison of experimental and computational data of the coordination environment in the Mg-polyP-30 complex: (A) Experimental X-ray scattering determined pair distribution function (PDF,  $G(r)$ ) both without (black) and with (red) reference solution correction. (B) Simulation determined radial distribution function (RDF,  $g(r)$ ) of Mg-polyP-30 overlaid with bars that mark the peaks in the RDFs for each individual Mg-O pairs. The gray boxes overlaid across both panels correspond to the ranges at which there are positive differences in the experimental data between the corrected and uncorrected PDF.

Furthermore, we employed the all atom-to-atom PDF obtained with the TXS measurements of the Mg-polyP-30 solution, which was corrected by the PDF of the reference  $MgCl_2$  solution to obtain experimental validation of the simulated coordination geometry of the

complexed Mg (Figure 1.5A). Since the only difference between the sample and reference solution was the presence of polyP-30, a positive difference between the uncorrected and corrected PDF was attributed to the complexation interaction between  $Mg^{2+}$  ions and polyP-30 (Figure 1.5A). Multiple correction factors (0.1, 0.3, 0.5, 0.7, and 0.9) were tested and they all yielded similar radial ranges at which there were positive differences between the uncorrected and corrected PDF for Mg with all O atoms (Figure S1.2). Selecting the correction factor of 0.7 for comparative analysis with the simulation results, we evaluated overlaps between the coordination distances of the polyP O atoms and the coordination distances with a positive difference in the experimentally determined PDF (Figure 1.5B). Remarkably, we found that all peaks in the simulated RDF for Mg-polyP-30 ligand O (occurring at radial distances of 1.71, 2.31, and 2.85 Å) were within the coordination distance ranges highlighted by the corrected total scattering PDF data (Figure 1.5B). The good agreement between the experimental and simulated coordination distances implied that the Mg complexation by both linear and circular forms of Mg-polyP-30 exhibited similar coordination geometry.

**3.4 Implications for the biological and environmental fates of metal-polyP complexes.** Previous studies have reported a correlation between EBPR performance and metal content in wastewaters, implying the dependence of phenotypic traits of PAOS for P removal on the type of metal-polyP complexes.<sup>3,7-14</sup> This correlation has been attributed commonly to the differential preferences amongst different PAOs for different metals serving as counterions to the negative charge of intracellular polyP.<sup>4,15</sup> However, the underlying mechanistic relationship between metal type and metal complexation by polyPs had largely remained unclear.

Our findings through molecular dynamics simulations predicted that the polyP complex with K was the least stable and the complex with Mg was the most stable, based on both the total

potential energies and coordination distances of the metal-polyP complexes investigated. The theoretical coordination geometry was subsequently confirmed by X-ray scattering analysis. Importantly, both Mg and K were reported previously to be co-localized with polyP granules of PAOs in EBPR activated sludge samples<sup>15</sup>, implying that the co-occurrence of metal-polyP complexes of different thermodynamic stability may be important to the physiological fate of polyP. In fact, the subsequent availability of the phosphate stored in polyP relies on phosphatase enzymes, which hydrolyze the terminal phosphate groups to release orthophosphate and thus shorten the polyP chain.<sup>29</sup> This enzymatic hydrolysis involves an intermediate chemical species wherein the polyP ligand O atoms complex divalent metal cations in the active site.<sup>30-33</sup> Therefore, the phosphate moieties in K-polyP complex with relatively lower chelation strength would be more available for the enzymatic hydrolysis to sustain a bioavailable physiological pool of polyP, whereas the relatively stronger Mg-polyP complex would be more appropriate for long-term polyP storage in the cell. In accordance with this proposal, the cellular Mg-polyP content was reported to have a statistically significant positive correlation to EBPR performance and stability.<sup>15</sup> For the underlying mechanism that governs such selective metal complexation by polyPs, our findings imply that the complexation of Mg is involved in establishing thermodynamically stable metal-polyP complexes.

Regarding the polyP configuration, the linear form of polyP has been considered the most common in all living organisms, while the biological synthesis and function of circular polyP are not well understood<sup>34,35</sup>. In biological samples, early studies have reported the coexistence of both forms of polyP, but the composition was deemed inconclusive due to errors in the extraction methods.<sup>35</sup> A recent study of the polyP content within *Xanthobacter autotrophicus* using the non-destructive <sup>31</sup>P solid-state nuclear magnetic resonance spectroscopy identified both linear and

cyclic polyP within cells.<sup>35</sup> Consistent with this latter finding, both linear and circular forms of Mg-polyP-30 complexes were found through our experimental size distribution analysis, obtained with both gel permeation chromatography and X-ray scattering, albeit the molecular simulations generated a circular structure for the Mg-polyP-30 complex. However, we obtained good agreements between the experimental PDF from the X-ray scattering data and the computed RDF from the molecular simulations, suggesting similar metal coordination geometry for both linear and circular configurations of Mg-polyP-30. For the metal complexes with the relatively shorter chain polyP (i.e., polyP<sub>10</sub>), only a (slightly curved) linear configuration was obtained, suggesting a polyP chain length threshold that facilitates transition between linear and circular configurations of the metal-polyP complexes. Elucidation of the biological significance of this structural transition warrants future investigation.

Activated sludge in EBPR systems is subjected to alternating anoxic and oxic conditions to favor and enrich PAOs for P removal.<sup>36,37</sup> Such fluctuating conditions, which can also be found in natural environments, have been implicated in PAO-involved P cycling in agricultural soil or sediments.<sup>3,4,38</sup> The new insights obtained here on the mechanism underlying the relationship between metal-polyP complexation and the behavior of PAOs in EBPR would also be relevant to P cycling and recycling in various natural habitats.<sup>3</sup> To extend the relevance of our findings to a variety of chemical and biological conditions, future research is needed to elucidate the molecular structure of complexes with other environmentally relevant metals and with polyPs of different chain lengths.

## **Acknowledgements**

This research was funded by a NSF CAREER grant awarded to L.A. from the U.S. National Science Foundation (NSF CBET-1653092). This work made use of the IMSERC Crystallography facility at Northwestern University, which has received support from the Soft and Hybrid Nanotechnology Experimental (SHyNE) Resource (NSF ECCS-2025633), and Northwestern University. Purchase of the Ag-microsource diffractometer used to obtain results included in this publication was supported by the Major Research Instrumentation Program (NSF CHE-1920248). The SAXS measurements were performed at the DuPont-Northwestern-Dow Collaborative Access Team (DND-CAT) located at Sector 5 of the Advanced Photon Source (APS). DND-CAT is supported by Northwestern University, The Dow Chemical Company, and DuPont de Nemours, Inc. This research used resources of the Advanced Photon Source, a U.S. Department of Energy (DOE) Office of Science User Facility operated for the DOE Office of Science by Argonne National Laboratory under Contract No. DE-AC02-06CH11357. The SAXS data were collected using an instrument funded by the National Science Foundation under Award Number 0960140

**CHAPTER 2**

**MULTIOMICS ANALYSIS OF NUTRIENT-DEPENDENT GROWTH AND  
BIOSYNTHETIC DEMAND FOR POLY( $\beta$ -HYDROXYBUTYRATE) IN *COMAMONAS  
TESTOSTERONI* KF-1**

Yeonsoo Park<sup>1,2</sup>, Rebecca A. Wilkes<sup>1,2</sup>, Jacob R. Waldbauer<sup>3</sup>, April Z. Gu<sup>4</sup>, Ludmilla Aristilde<sup>1,2</sup>

<sup>1</sup> Department of Biological and Environmental Engineering, College of Agriculture and Life Sciences, Cornell University, Ithaca, NY 14853 USA

<sup>2</sup> Department of Civil and Environmental Engineering, McCormick School of Engineering and Applied Science, Northwestern University, Evanston, IL 60208 USA

<sup>3</sup> Department of the Geophysical Sciences, University of Chicago, Chicago, IL 60637 USA

<sup>4</sup> Department of Civil and Environmental Engineering, College of Engineering, Cornell University, Ithaca, NY 14853 USA

## **1. Introduction**

Polyhydroxyalkanoates (PHAs) have been gaining interest as a source of biodegradable substitutes to conventional, petroleum-based plastics with similar thermal and mechanical properties.<sup>39-41</sup> Many prokaryotic microorganisms can naturally synthesize PHAs to serve as carbon and energy reserves.<sup>42</sup> Microbial accumulation of poly( $\beta$ -hydroxybutyrate) (PHB), a commonly found PHA, has been reported in many microorganisms when cells are grown in either excess carbon or limitation of nutrients such as nitrogen (N) and phosphorus (P).<sup>39,42,43</sup> In response to nutrient replenishment, the accumulated PHB gets subsequently degraded to be metabolized thus provide carbon and energy to the cell.<sup>39,44</sup>

Of special interest is *Comamonas testosteroni*, a bacterium commonly found in polluted environmental samples, that is capable of metabolizing and accumulating PHB.<sup>40,45,46</sup> Production of PHB in *C. testosteroni* has been investigated during feeding on different carbon sources and under different nutrient conditions.<sup>39,40</sup> Reduced N availability was identified as a trigger to

increased cellular PHB production.<sup>39,40</sup> Based on its genome, *C. testosteroni* does not possess the enzymes for either the assimilatory route for common sugars such as glucose or the complete oxidative pentose phosphate (PP) pathway.<sup>45,47</sup> Therefore, the functional pathways in the central carbon metabolism of this species are the Embden-Meyerhof-Parnas (EMP), Entner-Doudoroff (ED), non-oxidative PP pathways, and the tricarboxylic acid (TCA) cycle.<sup>45,47</sup> However, it is not yet understood how the central carbon metabolism is remodeled in response to nutrient limitations to achieve accumulation of PHB.

Here we investigated the nutrient-dependent relationship between PHB biosynthesis and cellular growth, metabolism, and energetics in *C. testosteroni* KF-1, towards elucidating the metabolic phenotypes favorable to PHB accumulation. First, we compared the biomass growth under varying acetate (as the carbon source), N, and P concentrations. Second, we performed a quantitative analysis of the N-dependent carbon metabolism, by supplying stable isotope tracers and metabolomics profiling using ultra-high-performance liquid chromatography (UHPLC) with high-resolution mass spectroscopy (HRMS). Third, we combined the quantitative metabolic flux analysis (MFA) and proteomics profiling to gain insight into the metabolic remodeling associated with PHB biosynthesis as a function of N availability. Fourth, we evaluated protein abundance change in key metabolic pathways relevant to PHB biosynthesis in response to decreasing P availability. Our findings revealed a threshold at which N depletion is favorable to PHB production compared to then replete conditions, as a result of imbalances between metabolic carbon flux and energetics due to compromised cellular growth.

## 2. Materials and Methods

**2.1 Materials.** The *C. testosteroni* KF-1 (DSMZ 14576) cells were obtained from Deutsche Sammlung für Mikroorganismen und Zellkulturen (Braunschweig, Germany). [ $^{13}\text{C}$ ] sodium acetate was obtained from Cambridge Isotopes (Tewksbury, MA); all other chemicals were obtained in analytical grade from Fischer Scientific (Pittsburg, PA) and Sigma-Aldrich (St. Louis, MO). All solutions were prepared with ultrapure water (Barnstead™ GenPure™ water purification system; Thermo Scientific; Waltham, MA) and filter-sterilized using 0.22  $\mu\text{m}$  polyethersulfone (PES) membranes filters (Millipore; Burlington, MA). Sample resuspensions for analysis were performed using LC-MS-grade water and filtered with 0.22  $\mu\text{m}$  cellulose acetate (CA) membrane filters (Corning; Corning, NY) prior to UHPLC-HRMS and nuclear magnetic resonance (NMR) analysis. The HRMS analysis was conducted using UHPLC (Thermo Scientific Dionex UltiMate 3000) coupled to a high-resolution accurate-mass spectrometer (Thermo Scientific Q Exactive quadrupole-Orbitrap hybrid) with electrospray ionization operated in negative mode. To quantify PHB (digested as crotonate), we used a UHPLC (Thermo Scientific Vanquish Flex with diode array detector). An Agilent Cary UV-visible spectrophotometer (Santa Clara, CA) was used for optical density readings at 600 nm ( $\text{OD}_{600}$ ) to monitor biomass growth. Cell biomass was also lyophilized with a freeze-dryer (FreeZone 2.5 Liter Benchtop Freeze Dryer; Labconco) to monitor cell dry weight in grams ( $\text{g}_{\text{CDW}}$ ).

**2.2 Culturing conditions and growth measurements.** The pH-adjusted ( $7.0 \pm 0.2$ ) and filter-sterilized minimal nutrient medium contained the following: 0.81 mM  $\text{MgSO}_4 \cdot 7\text{H}_2\text{O}$ , 8.6 mM NaCl, 34  $\mu\text{M}$   $\text{CaCl}_2 \cdot 2\text{H}_2\text{O}$ , 30  $\mu\text{M}$   $\text{FeSO}_4 \cdot 7\text{H}_2\text{O}$ , 0.86  $\mu\text{M}$   $\text{CuSO}_4 \cdot 5\text{H}_2\text{O}$ , 1.9  $\mu\text{M}$   $\text{H}_3\text{BO}_3$ , 7.7  $\mu\text{M}$   $\text{ZnSO}_4 \cdot 7\text{H}_2\text{O}$ , 0.75  $\mu\text{M}$   $\text{MnSO}_4 \cdot 5\text{H}_2\text{O}$ , 0.26  $\mu\text{M}$   $\text{NiCl}_2 \cdot 6\text{H}_2\text{O}$ , and 0.31  $\mu\text{M}$

$\text{Na}_2\text{MoO}_4 \cdot 5\text{H}_2\text{O}$ .<sup>48,49</sup> For all conditions, sodium acetate was fed as a sole carbon source at a concentration of 50 mM C. For the nutrient-replete (control) condition, 89.4 mM  $\text{K}_2\text{HPO}_4$ , 56.4 mM  $\text{NaH}_2\text{PO}_4$ , and 18.7 mM  $\text{NH}_4\text{Cl}$  were added. For the N-dependent condition, the  $\text{NH}_4\text{Cl}$  concentration was reduced by 10-fold (1.87 mM  $\text{NH}_4\text{Cl}$ ). For the P-dependent condition, the total  $\text{PO}_4^{3-}$  concentration, maintaining a constant  $\text{K}_2\text{HPO}_4/\text{NaH}_2\text{PO}_4$  ratio, was reduced by 100- and 500-folds corresponding to 1.46 mM and 0.29 mM total  $\text{PO}_4^{3-}$ , respectively. In addition, the elemental composition of *C. testosteroni* biomass was analyzed with the Elementar Vario EL Cube combustion analysis conducted by the Integrated Molecular Structure Education and Research Center (IMSERC) located in Northwestern University (Table 2.1).

*Comamonas testosteroni* KF-1 cells were initially grown in Luria-Bertani (LB) medium, mixed with 50% glycerol at mid-exponential phase, and then aliquots were stored at -80 °C in cryogenic vials. Vials were left to adjust to room temperature prior to transfer into the minimal nutrient growth medium, and a minimum of two transfers into the growth medium was used to acclimate cells to each specific growth condition. At each transfer step, cells were washed in the minimal-nutrient medium to minimize the transfer of carry-over carbon and nutrients from the previous culture. Cultures were grown in an incubator (model I24; New Brunswick Scientific, Edison, NJ) maintained at 30 °C and shaken at 220 rpm. Bacterial growth in 125- or 250-mL baffled Erlenmeyer flasks in three biological replicates was monitored as a function of time until late- stationary phase, using  $\text{OD}_{600}$ , where cell suspensions were diluted when the value was above 0.5 to obtain accurate readings. The  $g_{\text{CDW}}$  values were also determined throughout growth by lyophilizing the cell pellets as previously described.<sup>50</sup> The biomass growth rate of  $0.746 \pm 0.050 g_{\text{CDW}} \cdot \text{L}^{-1} \text{OD}^{-1}$  was obtained via regression analysis.

**2.3 Acetate consumption and extracellular nutrient measurements.** For all nutrient conditions, samples were obtained throughout growth (14 to 22 different time points) to monitor acetate consumption and metabolite secretion. Culture aliquots (1.5 mL; three biological replicates) were pelleted by centrifugation (10,000 rpm, 5 min, 4 °C), filtered, and stored at -20 °C until analysis. For quantifying acetate concentration by NMR analysis, 100  $\mu$ L of the filtered sample was mixed with 60  $\mu$ L of 100% D<sub>2</sub>O, 50  $\mu$ L of 10 mM sodium azide as an antimicrobial agent, 150  $\mu$ L of 6 mM 2,2-dimethyl-2-silapentane-5-sulfonate (DSS) as a chemical shift reference compound, and 240  $\mu$ L of 100 mM NaHCO<sub>3</sub> for pH control. The Bruker Avance III HD system equipped with a TXO 5 mm Prodigy probe w/ Z-Gradient available at IMSERC was used for the <sup>1</sup>H-NMR measurements and subsequent analysis of the obtained 1D proton spectrum was performed using the MestReNova (Mestrelab Research) software. Acetate consumption rates (in mmol·g<sub>CDW</sub><sup>-1</sup>h<sup>-1</sup>) were determined via regression analysis of acetate depletion over time combined with biomass growth rate. For the N- and P- dependent conditions, with the same filtered samples, the extracellular NH<sub>3</sub>-N and PO<sub>4</sub><sup>3-</sup> concentrations were monitored throughout growth using a commercially available NH<sub>3</sub>-N assay kit based on the salicylate method (TNT 832; HACH) and the phosphomolybdate spectrophotometric method, respectively.

**2.4 Metabolite Quantification.** All metabolite quantifications by UHPLC-HRMS followed a previously described protocol.<sup>48,49</sup> Briefly, an Acquity UPLC Waters column of 1.7  $\mu$ m particle size (2.1×100 mm; Milford, MA) was used for the UHPLC, setting a constant column temperature of 25 °C and a constant flow rate of 0.180 mL/min with the injection volume for each sample set to 10  $\mu$ L. The solvent compositions as described previously.<sup>48</sup> All metabolite identification and quantification were done with Thermo Scientific Xcalibur 3.0 Quan Browser.

*Extracellular metabolites.* Metabolite excretion was measured for the control and N-dependent condition by monitoring the extracellular metabolite levels in the cell-free samples prepared for acetate consumption measurements. Excretion rates (in  $\text{mmol}\cdot\text{g}_{\text{CDW}}^{-1}\cdot\text{h}^{-1}$ ) were calculated by regression analysis for the following metabolites relevant to the central carbon metabolism: glucose 6-phosphate (G6P), fructose 6-phosphate (F6P), fructose 1,6-bisphosphate (FBP), 3-phosphoglycerate (3PG), phosphoenolpyruvate (PEP), pyruvate (PYR), xylulose 5-phosphate (Xu5P), ribose 5-phosphate (R5P), sedoheptulose 7-phosphate (S7P), aspartate, citrate,  $\alpha$ -ketoglutarate ( $\alpha$ KG), succinate, fumarate, and malate.

*Intracellular metabolites.* For each nutrient condition, cells were sampled during the exponential growth phase and intracellular metabolites were extracted following the protocol described by Sawnow *et al.*<sup>50</sup> Briefly, aliquots (3 mL) were sampled (three biological replicates) and filtered through 0.22  $\mu\text{m}$  nylon filters. The cell-containing filter disks were immediately quenched in 2 mL of 4 °C methanol:acetonitrile:water solution (2:2:1) for 30 min. Lysed cell biomass was separated via centrifugation, and then supernatants were transferred to a separate centrifuge tube and dried down with ultra-high purity  $\text{N}_2$  gas. Once fully dried, the samples were stored at -20 °C until further analysis with LC-HRMS. When preparing samples for UHPLC-HRMS, the metabolites were resuspended in LC-MS-grade water at different volumes to obtain different dilution factors. For the long-term  $^{13}\text{C}$ -labeling of intracellular metabolites, 25% of the total acetate was supplied as  $[\text{U}-^{13}\text{C}]$  sodium acetate. and cells were sampled at two different time points during the exponential phase of each nutrient condition. The labeling  $^{13}\text{C}$ -labeling patterns for the central carbon metabolites listed previously were analyzed with the Metabolomic Analysis and Visualization Engine (MAVEN) software.<sup>51</sup> For all metabolites, the natural  $^{13}\text{C}$  abundance was accounted for by using the isotope correction for high-resolution MS labeling

experiments (IsoCor) software.<sup>52</sup> To verify pseudo-steady-state isotopic enrichment of the intracellular metabolites, we compared the isotope labeling pattern of all analyzed metabolites at the two different time points of each condition (Figure S2.4). Intracellular metabolite levels were quantified using samples retrieved at the second time point for the isotope labeling experiment for each condition. The aspartate labeling pattern was used as a proxy for oxaloacetate (OAA), a direct precursor to aspartate, by assuming equilibrium between the two metabolites.<sup>50</sup> The labeling of dissolved CO<sub>2</sub> was estimated by comparing the labeling patterns of aspartate to N-Carbamoyl-aspartate or aspartate to PYR (Figure S2.5).

**2.5 Intracellular PHB measurements.** Intracellular PHB was measured throughout the exponential phase for the control and N-dependent conditions to obtain the PHB production rates and at a single time point during the exponential phase for the P-dependent conditions to obtain the PHB levels. The samples were lyophilized and acid digested to measure the resulting crotonate with UHPLC as described by Padovani *et al.* with minor modifications to the procedure.<sup>53</sup> At time points within the exponential phase, 10 mL culture aliquots were pelleted via centrifugation (3,200 g, 10 min, 4 °C), washed with ultrapure water, lyophilized, and then stored in -20 °C until further analysis. Prior to analysis, cell pellets were digested at 90-95 °C in a silicone oil bath with 1 mL of H<sub>2</sub>SO<sub>4</sub> (concentrated) for 30 mins and filtered with 0.45- $\mu$ m polypropylene filters after cooled down cooling to room temperature. The digested and filtered samples were subjected to 5-fold dilution with ultrapure water and then analyzed with the UHPLC equipped with a ZORBAX Eclipse Plus C18 5- $\mu$ m column (4.6 $\times$ 100 mm; Agilent). The solvent composition and flow rate were both as previously stated.<sup>53</sup> The crotonate concentrations were analyzed with the Chromeleon 7 CDS software (Thermo Scientific) and the production rates (in  $\mu\text{mol}\cdot\text{g}_{\text{CDW}}^{-1}\text{h}^{-1}$ ) were determined by regression analysis.

**2.6 Quantitative MFA and co-factor balance for the N-dependent condition.** To elucidate the metabolic fluxes through the central carbon metabolism of *C. testosteroni* under the two N-dependent conditions, we compiled the <sup>13</sup>C-labeling patterns with the substrate consumption rates, metabolite secretion rates, growth rates, and cellular stoichiometry. Carbon effluxes from the biomass precursor metabolites were estimated based on the reported biomass composition of *Pseudomonas testosteroni* (proteins, nucleic acids, cell membrane, and carbohydrate polymers), adjusted by the substrate consumption and growth phenotype of each condition.<sup>54,55</sup> The model metabolic network for *C. testosteroni* KF-1 was constructed by referencing the metabolic pathways predicted by MetaCyc<sup>56</sup> and the draft genome sequence for this strain.<sup>45</sup> The following reactions were constrained in the forward direction: F6P → G6P, FBP → F6P, and PEP → 3PG. Optimized fluxes in the metabolic model were simulated with the OpenFLUX2 software, whereby *in silico* <sup>13</sup>C-labeling patterns of targeted metabolites were computed iteratively with the input measured labeled fractions.<sup>57</sup> Upon flux optimization, the 95% confidence intervals of the fluxes were computed via a Monte Carlo-based approach.<sup>57</sup> Each MFA was performed the experimental <sup>13</sup>C-labeling patterns of each replicate. We used the computed metabolic fluxes to estimate the production and consumption rates of cofactors: adenosine triphosphate (ATP), nicotinamide adenine dinucleotide (NADH), ubiquinone (UQ), and nicotinamide adenine dinucleotide phosphate (NADPH).

**2.7 Proteomics.** For all nutrient conditions, proteomics analysis was done on four biological replicates by sampling cells during the exponential phase. At OD<sub>600</sub> values corresponding to those of the second time point for the isotope labeling experiment described above, 15 mL of the culture was sampled, pelleted via centrifugation (3,200 g, 10 min, 4 °C), and stored at -80 °C until further analysis. The quantification of the proteome of each sample

followed the protocol described by Waldbauer *et al.*<sup>58</sup> From all the proteins measured, we removed proteins that were identified in less than three of the four replicates or had less than five isobaric peptide terminal labeling MS2 spectra. Then, significantly differential protein expression between the different conditions was determined by calculating the z-score for protein abundance differences by taking the difference in the log<sub>2</sub>-transformed mean protein abundance between conditions. These values were subsequently divided by the sum of the total uncertainty estimate for the protein in the two conditions being compared. The obtained total uncertainty estimate for a given condition was calculated with the following equation: square root of the sum of the standard deviation of a protein's abundance and the average standard error of the protein's abundance across qualified spectra within each replicate. Finally, these z-scores were converted to *p*-values assuming a standard normal distribution and then the familywise error rate for significantly differential expression between conditions was controlled to 0.05 using the *q*-value method to correct for multiple testing.<sup>58</sup> In addition, we analyzed the relative abundance of the proteins relevant to the central carbon metabolism or nutrient metabolism by comparing the log<sub>2</sub>-transformed relative abundance results of the N- and P-dependent conditions to those of the control condition. For the analysis, we focused on the proteins that had an increase or decrease greater than 0.3-fold in each nutrient-dependent condition compared to the control condition.

**2.8 Metabolite level and relative protein abundance visualization.** For the metabolite level analysis, we first corrected the quantified metabolite concentrations by the OD<sub>600</sub> values of the sampling time point. Then, the values for each nutrient condition were normalized by that of the control condition and log<sub>2</sub>-transformed. To compare the relative abundance of the identified proteins that are relevant to the central carbon, N, and P metabolism, we calculated the differences in the log<sub>2</sub>-transformed relative protein abundances for each nutrient condition and

the control. These values were input to Java TreeView version 1.1.6r4 to prepare the heat maps in Figure 2.5B and C.<sup>59</sup>

### 3. Results and Discussion

**3.1 Growth response of *C. testosteroni* KF-1 to nutritional availability of N and P.** Due to reported bacterial growth inhibition by acetate,<sup>60</sup> we first investigated the effect of acetate concentration on the growth rate of *C. testosteroni* (Figure 2.1; Figure S2.1). The growth rates were  $0.26 \pm 0.01$ ,  $0.34 \pm 0.00$ ,  $0.42 \pm 0.02$ , and  $0.34 \pm 0.01$  h<sup>-1</sup>, when the cells were grown on 10, 25, 50, and 100 mM C acetate, respectively (Figure 2.1; Figure S2.1). The growth rates for all conditions, except 25 mM C compared to 100 mM C, had statistically significant differences ( $p < 0.05$ ) (Figure 2.1). All following experiments were performed with 50 mM C acetate, which led to the highest growth rate.

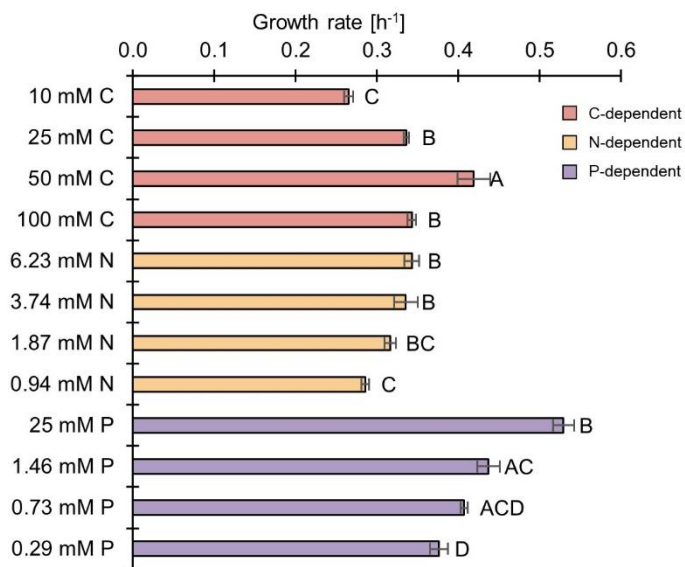


**Figure 2.2** Growth rates for *C. testosteroni* KF-1 fed on acetate as a sole carbon source with varying nutrient concentrations: different acetate concentrations with 18.7 mM NH<sub>4</sub>Cl and 145.8 mM PO<sub>4</sub> (red), different NH<sub>4</sub>Cl concentrations with 50 mM C acetate and 145.8 mM PO<sub>4</sub> (yellow), and different total PO<sub>4</sub> concentrations with 50 mM C acetate and 18.7 mM NH<sub>4</sub>Cl (purple). Significant differences ( $p < 0.05$ ) are denoted by changes in letters. Data are shown as mean  $\pm$  standard deviation for biological replicates ( $n = 3$ ).

To decide on the nutrient concentrations for the N- and P-dependent conditions, we first investigated the effect of N and total P concentration on cell growth (Figure 2.1; Figure S2.1). The growth rates were  $0.34 \pm 0.01$ ,  $0.34 \pm 0.01$ ,  $0.32 \pm 0.01$ , and  $0.29 \pm 0.00 \text{ h}^{-1}$  in response to 3-, 5-, 10-, and 20-fold decrease in N concentration compared to the control condition, respectively (Figure 2.1; Figure S2.1). When the N concentration was reduced by 3-fold, the growth rate decreased by nearly 20% compared to the control condition, but further N depletions were statistically insignificant ( $p > 0.10$ ) (Figure 2.1). Interestingly, during the 10- and 20-fold reductions in N, we observed a diauxic growth trend whereby the growth rate of the second phase was 83% less than the growth rate of the first phase (Figure S2.1; Figure S2.3); only the growth rates for the first growth phase were illustrated in Figure 2.1.

With respect to growth responses to P depletion, the growth rates were  $0.53 \pm 0.01$ ,  $0.44 \pm 0.01$ ,  $0.41 \pm 0.00$ , and  $0.38 \pm 0.01 \text{ h}^{-1}$  when the total P concentration was 6-, 100-, 200-, and 500-fold less than the replete condition, respectively (Figure 2.1; Figure S2.1). When the total P concentration decreased to 25 mM from the replete condition, the growth rate increased. When the concentration was reduced by 100-folds, the difference in growth rates was statistically insignificant, but a further reduction by 300-folds had a statistically significant difference (Figure 2.1). Interestingly, though such differences in growth rates (ranging from  $0.09$  to  $0.15 \text{ h}^{-1}$ ) were observed, there was less than about 12% difference in the maximum biomass across all tested concentrations (Figure S2.1). Therefore, *C. testosteroni* KF-1 seems to be more sensitive to N depletion than P depletion.

**Table 2.1** Elemental composition of biomass in % (weight/weight)

	C	N	H	S	O	P
<i>C. testosteroni</i> KF-1 <sup>a</sup>	$43.9 \pm 0.2$	$13.0 \pm 0.2$	$7.2 \pm 0.0$	$0.5 \pm 0.0$	-	-
<i>P. putida</i> KT2440 <sup>b</sup>	48.8	15.2	6.2	0.7	26.4	2.7

<sup>a</sup>From this study (mean  $\pm$  standard deviation,  $n = 3$ )

<sup>b</sup>From Duuren *et al.* 2013

To estimate the cell stoichiometric N and P requirement, we conducted a combustion analysis of *C. testosteroni* KF-1 biomass which gave the weight-by-weight percentage of C, H, N, and S content (Table 2.1). Because this analysis does not provide information on P, we referenced a paper that reported the elemental composition for *Pseudomonas putida* KT2440, given that *C. testosteroni*, which has previously been classified as *Pseudomonas*, is phylogenetically related.<sup>47,61,62</sup> By considering the biomass conversion rate and maximum OD<sub>600</sub> of the nutrient replete condition, we calculated the stoichiometrically required N and P concentrations to be 13.2 mM N and 1.13 mM P. Therefore, we confirmed that the control was replete in N and P. Moreover, we confirmed that the 10-fold N reduction and 500-fold P reduction from the control would be below the stoichiometric N and P requirement, respectively. We attributed the unexpected diauxic growth trend during the 10-fold reduction in available N to a response to more severe N limitation than at the start of the growth curve. To further investigate this case, we selected the 10-fold N reduced condition as our N-dependent condition. For the P-dependent investigation, we chose the 100- and 500-fold reductions of available P relative to the control condition. By monitoring the kinetic extracellular NH<sub>3</sub>-N or phosphate concentrations of these selected growth conditions, we found complete depletion of N and P for 10-fold N reduction and 500-fold P reduction, respectively. In agreement with the theoretical estimations of P requirement, P depletion was not complete for the 100-fold P reduction but rather reached a concentration plateau (Figure S2.2). Interestingly, the acetate consumption rates were all comparable ( $p > 0.05$ ) across all nutrient conditions, except for the second growth phase of the N-dependent condition for which the acetate consumption was decreased significantly by nearly 80% compared to the first phase (Figure S2.3). We sought to understand how intracellular carbon metabolism is altered to respond to changes in nutrient (N and P) availability.

### 3.2 Changes in metabolic pathways and fluxes in response to reduced N-availability.

Using  $^{13}\text{C}$ -labeling data, we conducted a quantitative MFA of *C. testosteroni* during the first growth phase of the N-dependent condition (denoted N1) and the second phase of the diauxic growth (denoted N2) (Figure 2.2). A discrepancy in the  $^{13}\text{C}$ -labeling patterns for several metabolites for N1 between the two measurements was likely due to the low biomass hence, low metabolite levels, which can contribute to error in labeling measurements (Figure S2.4). Metabolite secretion was detected for PYR ( $0.013 \pm 0.010 \text{ mmol}\cdot\text{g}_{\text{CDW}}^{-1}\text{h}^{-1}$ ) and  $\alpha\text{KG}$  ( $0.281 \pm 0.086 \text{ mmol}\cdot\text{g}_{\text{CDW}}^{-1}\text{h}^{-1}$ ) in the N2 condition (Table S2.2).

Overall, the absolute metabolic fluxes decreased with decreasing N levels (Figure 2.2). However, the absolute values do not account for the difference in growth rates and acetate consumption rates across the conditions (Figure 2.1; Figure S2.3). Therefore, we considered the z-scores of each metabolic reaction to highlight the increase and decrease compared to the control condition (Figure 2.2). The relative differences in the acetate consumption rates of N1 and N2 were reflected in the relative changes in the metabolic fluxes of the canonical TCA cycle (Figure 2.2), but flux through the glyoxylate shunt had a pronounced decrease as a function of decreasing N levels (Figure 2.2). The glyoxylate shunt is considered essential for bacterial growth on acetate (or fatty acids) as a carbon source under conditions due to the requirement for gluconeogenesis.<sup>63</sup> Therefore, it was intriguing to observe decreased flux through the glyoxylate shunt (by 30% and 40% for N1 and N2, respectively, each compared to the control) along with a decrease in fluxes to the upper metabolism (EMP, ED, and non-oxidative PP pathway). For all reactions above PEP, the fluxes remained steady for N1 relative to the control (with about 13% decreases) but decreased significantly by about 93% during N2 when extracellular N was completely depleted (Figure 2.2). In accordance with the aforementioned decrease in growth

rate, the biomass effluxes for N2 were all decreased compared to the N1 phase and the control (Figure 2.2). Considering that the role of the glyoxylate shunt is to funnel carbon to anabolism before carbon loss through the oxidative side of the TCA cycle, the reduction of carbon away from the glyoxylate shunt needed to be resolved. Beyond the metabolite secretion rates of PYR and  $\alpha$ KG during N2, which were very small, there was an increased flux (by 13%) from acetyl-CoA to PHB during N1 (Figure 2.2). We also evaluated the intracellular metabolite levels and protein abundances to elucidate the underlying regulation.

Among the total proteins analyzed ( $n = 453$ ), about 0.3% and 1.6% had a statistically significant difference when comparing N1 and N2 to the control, respectively. For the relative protein abundances (in circles in Figure 2.2), we found general agreement with the relative increase and decrease in the metabolic fluxes of N1 and N2, relative to the control. The flux to the glyoxylate shunt was decreased by 30 – 40% with decreasing N levels, while the relative abundance of isocitrate lyase (AceA) (which catalyzes the first reaction in the shunt to produce glyoxylate and succinate from citrate) was also decreased by 20% and 60% for N1 and N2, respectively (Figure 2.2). The abundance of PEP carboxykinase (PckA), which catalyzes the conversion of OAA to PEP, decreased noticeably by 70%, during N2, consistent with the decrease in the corresponding metabolic flux (Figure 2.2). Interestingly, despite a relative increase by 50% and decrease by 53% in the metabolic flux to citrate during N1 and N2, respectively, the relative abundance of aconitase hydratase (AcnB) did not change significantly for either condition (Figure 2.2). Similarly, the relative abundance for succinate dehydrogenase (SdhC) and malate dehydrogenase (Mdh) remained steady despite changes in the associated metabolic fluxes in the TCA cycle (Figure 2.2). Instead, elevated levels of acetyl-CoA and succinate by 244% and 106%, respectively, in N2 than in N1 coupled with the secretion of

metabolites (PYR and  $\alpha$ KG) reflected a bottleneck at these two metabolic nodes of the metabolic pathway (Figure 2.2).

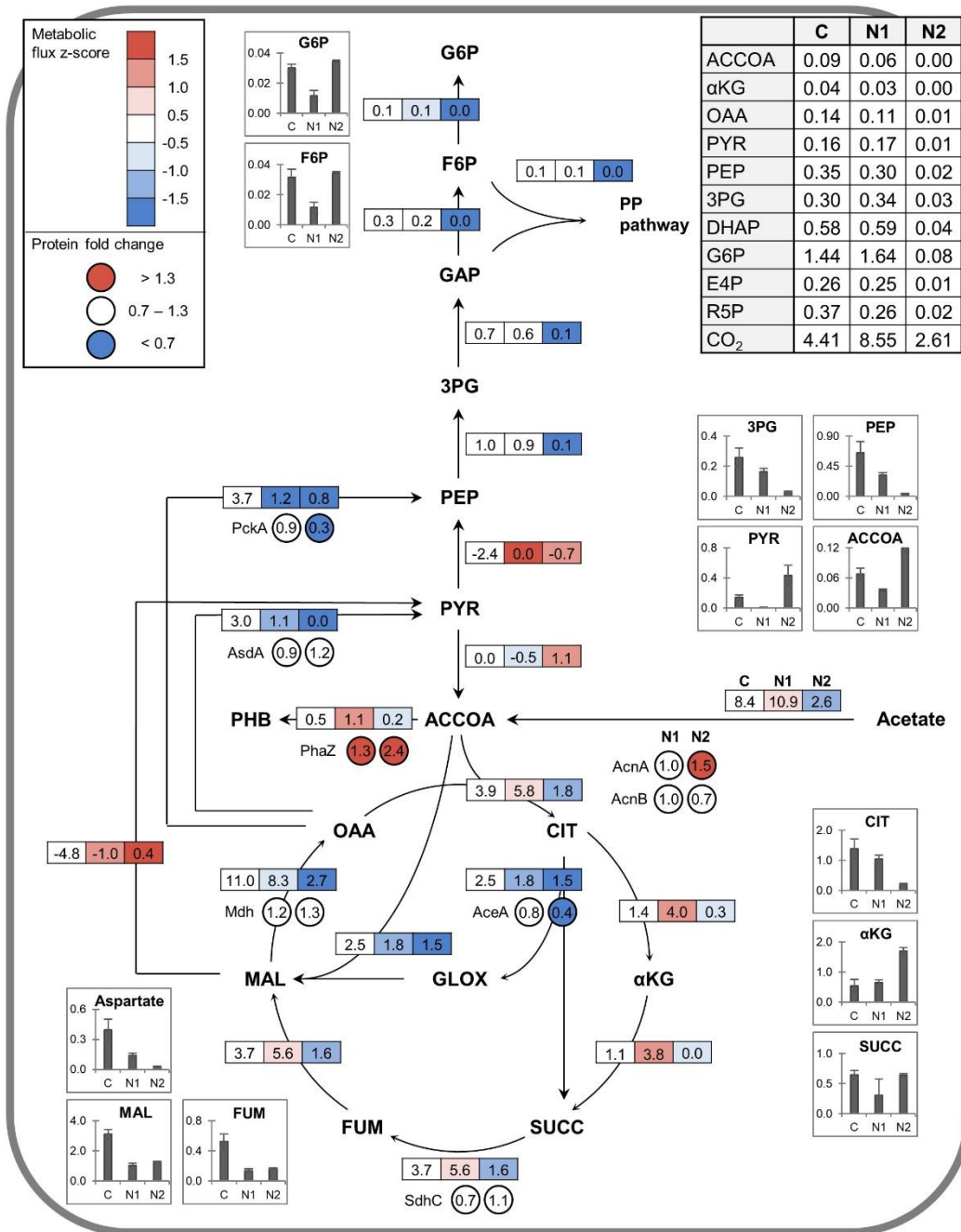


**Figure 2.3** Schematic of carbon metabolism in *C. testosteroni* KF-1 under the control and N-dependent condition. Boxes next to each arrow hold the average absolute fluxes (in  $\text{mmol}\cdot\text{g}_{\text{CDW}}^{-1}\cdot\text{h}^{-1}$ ) of the control (C), N-dependent condition phase 1 (N1), and phase 2 (N2), consecutively. Circles under selected fluxes hold the X-fold change of the named proteins for the N1 and N2 respective to C. For both the metabolic fluxes and the proteomics results, increases compared to the C condition are marked with red, and decreases are marked with blue. The absolute biomass effluxes (in  $\text{mmol}\cdot\text{g}_{\text{CDW}}^{-1}\cdot\text{h}^{-1}$ ) for all three conditions are listed in the table in the upper right corner. The bar graphs show the intracellular metabolite levels in the three conditions (mean  $\pm$  standard deviation,  $n = 3$ ) near the position of the measured metabolite in the reaction scheme. Abbreviations: glucose 6-phosphate (G6P), fructose 6-phosphate (F6P), glyceraldehyde 3-phosphate (GAP), 3-phosphoglyceric acid (3PG), phosphoenolpyruvate (PEP), pyruvate (PYR), acetyl-CoA (ACCOA), citrate (CIT),  $\alpha$ KG ( $\alpha$ -ketoglutarate), succinate (SUCC), fumarate (FUM), malate (MAL), oxaloacetate (OAA), dihydroxyacetone phosphate (DHAP), erythrose 4-phosphate (E4P), ribose 5-phosphate (R5P), poly( $\beta$ -hydroxybutyrate) (PHB).

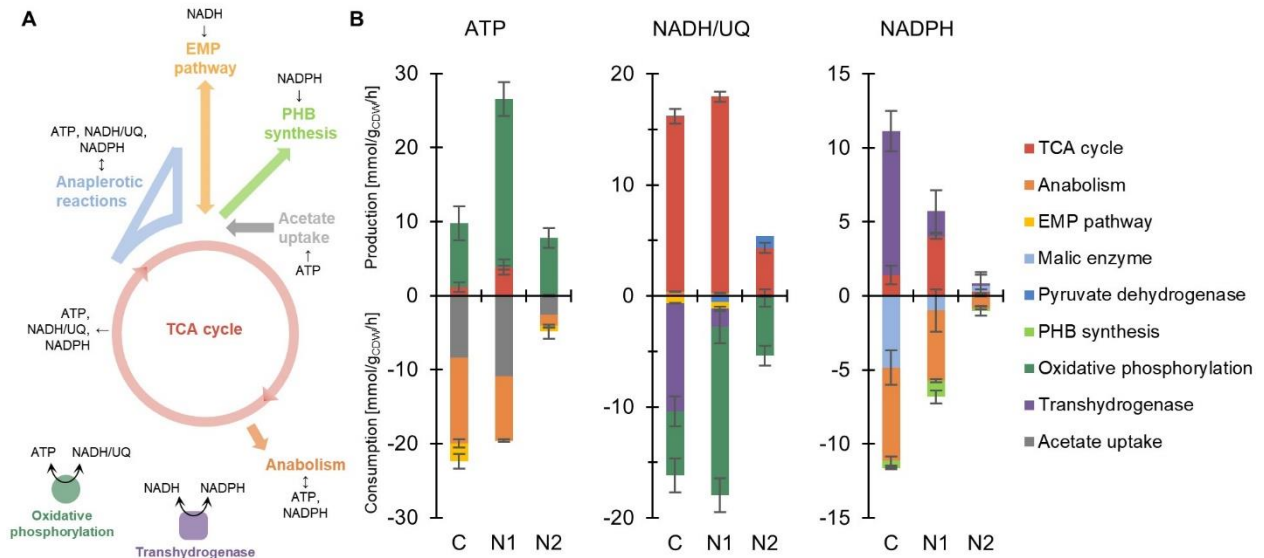


**Figure 4.** Cofactor balances for the control (C), N-dependent condition phase 1 (N1), and phase 2 (N2): (A) schematic of the energy metabolism in the carbon metabolism and (B) consumption and production balances for ATP, NADH/UQ, and NADPH estimated by the MFA flux results for the control and N-dependent conditions. Data presented are the average  $\pm$  standard deviation of the best-fit fluxes. Abbreviations: adenosine triphosphate (ATP), nicotinamide adenine dinucleotide (NADH), ubiquinone (UQ), nicotinamide adenine dinucleotide phosphate (NADPH).

Accordingly, the increased flux to PHB (by 13%) during N1 would route carbon from the metabolic bottleneck to acetyl-CoA, but there was a subsequent decrease in the flux to PHB (by 64%) during N2 (Figure 2.2). However, the level of the protein [PHB depolymerase (PhaZ)] involved in the PHB biosynthesis increased by 84% from N1 to N2 (Figure 2.2). To probe the reason for this discrepancy, we examined the cofactor balances (Figure 2.3). Across the three conditions, the major source of ATP production was through oxidative phosphorylation, which correspondingly was the major source of NADH/UQ consumption (Figure 2.3). It was also noticed that NADH/UQ were primarily produced through the TCA cycle (Figure 2.3). Both ATP and NADPH levels produced were depleted by 71% and 85%, respectively, from N1 to N2, which could be disadvantageous to fulfilling the NADPH requirement of PHB biosynthesis (Figure 2.3B).<sup>39</sup> Therefore, the flux to PHB may have decreased due to limitations imposed by the energy metabolism. Remarkably, there was an overall ATP deficit under the control

condition whereas there was an overall ATP surplus under both N-dependent conditions (Figure 2.3B), consistent with previous studies that suggested that PHB serves as not only carbon but also energy storage.<sup>41</sup>

**3.3 Nitrogen metabolism.** We evaluated the metabolite levels and protein abundances relevant to  $\text{NH}_3$  assimilation in response to N depletion. The three enzymes relevant to  $\text{NH}_3$  assimilation are glutamine synthetase (GS), glutamate synthase (GOGAT), and glutamate dehydrogenase (GDH) (Figure 2.4). Via the GS/GOGAT pathway or the GDH pathway,  $\text{NH}_3$  is assimilated to either glutamate or glutamine. Despite a higher energy cost for the GS/GOGAT pathway compared to the GDH pathway, the GS/GOGAT pathway is the preferred assimilation route at low N levels because GS has a higher affinity to  $\text{NH}_3$ .<sup>64</sup> Accordingly, the protein abundances of GlnA and GlnK, both of which are associated with the GS pathway, continued to increase with decreasing N levels, and eventually increased by 5.4- and 44.4-fold, respectively, for N2 compared to the control (Figure 2.4). The abundances of GltB and GltD in the GOGAT pathway also increased both by 2.5-folds during N1 and by 1.5- and 2.1-fold, respectively, during N2 compared to the control (Figure 2.4). Moreover, the enzymes relevant to the GDH pathway showed insignificant change compared to the control and hence were not depicted in Figure 2.4. Consistent with the greater increase of the proteins in the GS pathway for the conversion of glutamate to glutamine than the proteins in the GOGAT pathway in the reverse direction, the glutamate pool size was continuously decreased with N depletion while the  $\alpha\text{KG}$  levels continued to increase (Figure 2.4). The glutamate levels were decreased by 59% from the control to N1 and by 58% from N1 to N2, whereas the  $\alpha\text{KG}$  levels increased by 20% and 163%, subsequently, with depleting N levels (Figure 2.4). Therefore, it was implied that the secretion of  $\alpha\text{KG}$  during N2 was caused by changes in the  $\text{NH}_3$  assimilation pathway induced by the reduced

N availability. Such effect of the N availability on  $\alpha$ KG, a TCA cycle metabolite, likely induced further changes in the carbon metabolism that led to reduced flux to PHB production during N2.

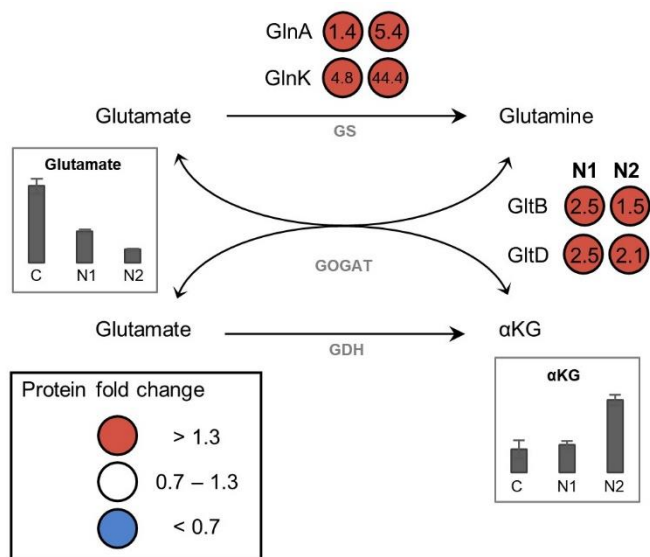


**Figure 2.5** Schematic of ammonium assimilation. Circles next to the metabolic reactions hold the X-fold increase values of the named proteins for the N1 and N2 respective to that of C. Increases in relative protein abundance compared to that of the C condition are marked with red and decreases are marked with blue according to the color scheme. Abbreviations: glutamine synthetase (GS), glutamate synthase (GOGAT), glutamate dehydrogenase (GDH),  $\alpha$ KG ( $\alpha$ -ketoglutarate).

**3.4 Nutrient-dependent metabolome and proteome changes.** We also compared the metabolite levels and relative protein abundances of the different nutrient conditions. For the comparison, we denoted the 100- and 500-fold P reduction conditions as P1 and P2, respectively. For the P-dependent conditions, among the total proteins analyzed ( $n = 507$ ), about 3.2% and 1.9% had a statistically significant difference when comparing P1 and P2 to the control, respectively. When comparing the intracellular PHB levels across the five nutrient conditions, the level was greatest for N2 and lowest for the control condition. Though the PHB levels for the N-dependent conditions may seem contrary to the metabolic flux analysis that showed a reduced flux from acetyl-CoA to PHB during N2, it is possible that the PHB level quantified in N2 reflected the accumulated amount throughout N1 and N2 while the flux itself had decreased by the time point of analysis (Figure 2.5A). Contrary to the N-dependent conditions where the PHB

level showed a steep increase by 12.5-fold between the two phases, the PHB levels for the P-dependent conditions remained constant (Figure 2.5A). Nonetheless, results showed that reduced P availability also induced greater PHB production (increased by 5.9-fold compared to the control) (Figure 2.5A).

There were several metabolic bottlenecks in the EMP pathway in response to P-deficiency that were absent in the N-dependent conditions (Figure 2.5B). Specifically, two metabolites (G6P and F6P) in the upper EMP pathway were elevated by 9- and 4.3-fold, respectively, compared to the control, whereas these metabolite pools remained relatively unchanged in the N-dependent conditions (Figure 2.5B). For metabolites involved in anaplerotic reactions (pyruvate and acetyl-CoA), there was a metabolic bottleneck that was also observed for N<sub>2</sub>, but the metabolite pool sizes of these metabolites were larger by 2- and 11.6-fold, respectively, for the P-dependent conditions than in N<sub>2</sub> (Figure 2.5B). All other metabolite levels of the P-dependent conditions were comparable to the control condition (Figure 2.5B).

Moreover, the relative protein abundances of proteins involved in the central carbon metabolism, N metabolism, and P metabolism during the nutrient-deplete conditions compared to the nutrient-replete condition are presented in Figure 2.5C. Contrary to the higher PHB levels quantified in the P-dependent conditions compared to the control, PhaZ abundances in P-dependent conditions and the control were comparable (Figure 2.5A and C). Furthermore, four proteins relevant to P metabolism (PhoH, UgpB, PstS, and Ppa) were identified for the P-dependent conditions (Figure 2.5C). Among the four proteins, only the relative abundance of PstS increased significantly (by 4.7-fold) during P<sub>2</sub> compared to the control (Figure 2.5C). The increased PstS abundance during the P-reduced condition agrees with the current knowledge on P acquisition pathways in bacteria; while the phosphate inorganic transporters (Pit) assimilate

phosphate under P-replete conditions, the phosphate-specific transport (Pst) system, which includes PstS, is induced under P-deplete conditions.<sup>65</sup> However, the steady levels of PhoH was unexpected since many genes involved in the P metabolism are controlled by the global regulatory phosphate (*pho*) regulon and PhoH is predicted to be an ATPase that is induced by P starvation.<sup>66</sup> Both the metabolite pool sizes and relative protein abundance data suggested that the carbon metabolism in *C. testosteroni* likely responds differently to reduced P- and N-availability.

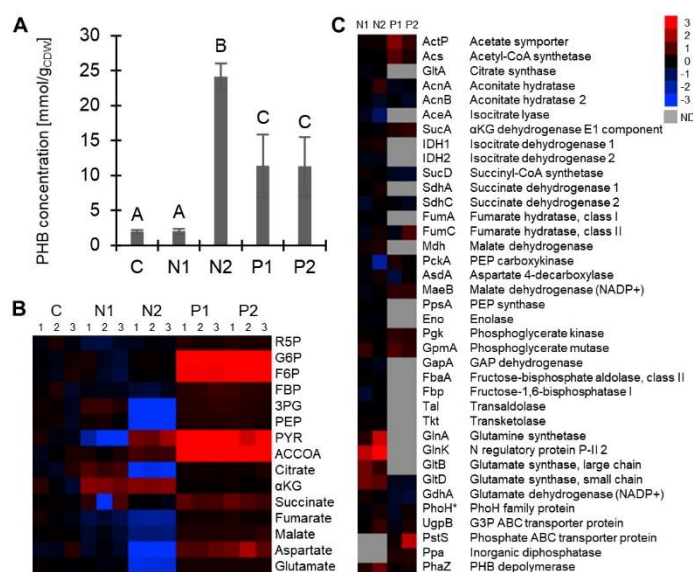


**Figure 2.5** Nutrient dependent (A) PHB levels, (B) metabolome profiling, and (C) proteome profiling for the five nutrient conditions: control (C), N-dependent condition phase 1 (N1) and phase 2 (N2), 100-fold P reduction condition (P1), and 500-fold P reduction condition (P2). Significant differences ( $p < 0.05$ ) denoted by changes in letters in panel A. The color scale for both heatmaps in panels B and C was based on  $\log_2$ -transformed values. Abbreviations: ribose 5-phosphate (R5P), glucose 6-phosphate (G6P), fructose 6-phosphate (F6P), 3-phosphoglyceric acid (3PG), phosphoenolpyruvate (PEP), pyruvate (PYR), acetyl-CoA (ACCOA),  $\alpha$ KG ( $\alpha$ -ketoglutarate), poly( $\beta$ -hydroxybutyrate) (PHB), not detected (ND).

#### 4. Conclusion

Poly( $\beta$ -hydroxybutyrate), an attractive source of bioplastic with shared physical properties with synthetic plastics, is known to accumulate naturally in environmental microorganisms subjected to the right nutrient availability conditions. However, there has been a lack of mechanistic understanding of carbon and N metabolisms responsible for promoted PHB

biosynthesis in bacteria. Using quantitative  $^{13}\text{C}$ -MFA combined with metabolomics and proteomics data, we elucidated important metabolic changes in response to N depletion. When grown on low N concentrations, *C. testosteroni* exhibited a greater flux of PHB production and, once the extracellular N was fully depleted, imbalances in energy metabolism during compromised biomass growth, the carbon flux was routed away from the glyoxylate shunt and PHB biosynthesis towards anaplerotic reactions and metabolic flux through reactions of  $\alpha\text{KG}$  and PYR from the TCA cycle. Comparison of the metabolite pool sizes and relative protein abundances for different N- and P-availability conditions highlighted the difference in the cells' response to N- and P-deficiencies. Results implied that the carbon metabolism would be remodeled differently in response to the two nutrient availability conditions.

However, the comparison of the metabolite and proteomics profiling results among the studied condition does not fully explain how the carbon metabolism is affected by P-deficiency and how it induces PHB accumulation. Therefore, future research on metabolic flux changes during P-dependent conditions through a similar quantitative  $^{13}\text{C}$ -MFA would allow a more comprehensive comparison between the two nutrient-dependent responses of *C. testosteroni*. Moreover, because environmental and engineered systems in which *C. testosteroni* can be subjected to can have various and more complicated nutrient availability conditions, an analysis across a wider range of nutrient conditions would enable further optimization of the bacteria's natural ability to synthesize PHB and provide guidance to any potential metabolic engineering on the strain to produce PHB. Nonetheless, our findings shed light on how the carbon metabolism underlying nutrient limitations can be optimized in environmental bacteria to favor PHB biosynthesis, as well as informing potential metabolic engineering strategies.

## REFERENCES

1. Kornberg, A. Inorganic polyphosphate: toward making a forgotten polymer unforgettable. *J. Bacteriol.* **177**, 491 (1995).
2. Müller, W. E. G., Schröder, H. C. & Wang, X. Inorganic polyphosphates as storage for and generator of metabolic energy in the extracellular matrix. *Chem. Rev.* **119**, 12337–12374 (2019).
3. Akbari, A. *et al.* Unrevealed roles of polyphosphate-accumulating microorganisms. *Microb. Biotechnol.* **14**, 82–87 (2021).
4. Saia, S. M., Carrick, H. J., Buda, A. R., Regan, J. M. & Walter, M. T. Critical Review of Polyphosphate and Polyphosphate Accumulating Organisms for Agricultural Water Quality Management. *Environ. Sci. & Technol.* **55**, 2722–2742 (2021).
5. Yang, Y., Shi, X., Ballent, W. & Mayer, B. K. Biological Phosphorus Recovery: Review of Current Progress and Future Needs: Yang *et al.* *Water Environ. Res.* **89**, 2122–2135 (2017).
6. Yuan, Z., Pratt, S. & Batstone, D. J. Phosphorus recovery from wastewater through microbial processes. *Curr. Opin. Biotechnol.* **23**, 878–883 (2012).
7. Imai, H., Endoh, K. & Kozuka, T. Magnesium requirement for biological removal of phosphate by activated sludge. *J. Ferment. Technol.* **66**, 657–666 (1988).
8. Rickard, L. F. & McClintock, S. A. Potassium and magnesium requirements for enhanced biological phosphorus removal from wastewater. *Water Sci. Technol.* **26**, 2203–2206 (1992).
9. Schönborn, C., Bauer, H.-D. & Röske, I. Stability of enhanced biological phosphorus removal and composition of polyphosphate granules. *Water Res.* **35**, 3190–3196 (2001).

10. Liu, W.-T. *et al.* In situ identification of polyphosphate-and polyhydroxyalkanoate-accumulating traits for microbial populations in a biological phosphorus removal process. *Environ. Microbiol.* **3**, 110–122 (2001).
11. Choi, H.-J., Yu, S.-W., Lee, S.-M. & Yu, S.-Y. Effects of potassium and magnesium in the enhanced biological phosphorus removal process using a membrane bioreactor. *Water Environ. Res.* **83**, 613–621 (2011).
12. Gu, A. *et al.* Evaluation of metal cation stoichiometry with biological phosphorus removal in full-scale EBPR processes. *Proc. Water Environ. Fed.* **2004**, 176 (2004).
13. Lindrea, K. C., Pigdon, S. P., Boyd, B. & Lockwood, G. A. Biomass characterization in a nitrification-denitrification biological enhanced phosphorus removal (NDBEPR) plant during start-up and subsequent periods of good and poor phosphorus removal. *Water Sci. Technol.* **29**, 91–100 (1994).
14. Brdjanovic, D., Hooijmans, C. M., Van Loosdrecht, M. C. M., Alaerts, G. J. & Heijnen, J. J. The dynamic effects of potassium limitation on biological phosphorus removal. *Water Res.* **30**, 2323–2328 (1996).
15. Li, Y. *et al.* The composition and implications of polyphosphate-metal in enhanced biological phosphorus removal systems. *Environ. Sci. Technol.* **53**, 1536–1544 (2018).
16. Ikotun, O. F., Marino, N., Kruger, P. E., Julve, M. & Doyle, R. P. Coordination complexes incorporating pyrophosphate: Structural overview and exploration of their diverse magnetic, catalytic and biological properties. *Coord. Chem. Rev.* **254**, 890–915 (2010).
17. Sharmin, N. & Rudd, C. Structure , thermal properties , dissolution behaviour and biomedical applications of phosphate glasses and fibres : a review. *J. Mater. Sci.* **52**, 8733–8760 (2017).

18. Sun, H. *et al.* COMPASS II: extended coverage for polymer and drug-like molecule databases. *J. Mol. Model.* **22**, 1–10 (2016).
19. Gras, P. *et al.* Crystal structure of monoclinic calcium pyrophosphate dihydrate (m-CPPD) involved in inflammatory reactions and osteoarthritis. *Acta Crystallogr. Sect. B Struct. Sci. Cryst. Eng. Mater.* **72**, 96–101 (2016).
20. Aristilde, L. & Sposito, G. Molecular modeling of metal complexation by a fluoroquinolone antibiotic. *Environ. Toxicol. Chem. An Int. J.* **27**, 2304–2310 (2008).
21. Pochodylo, A. L., Klein, A. R. & Aristilde, L. Metal-binding selectivity and coordination dynamics for cyanobacterial microcystins with Zn, Cu, Fe, Mg, and Ca. *Environ. Chem. Lett.* **15**, 695–701 (2017).
22. Momeni, A. & Filiaggi, M. J. Synthesis and characterization of different chain length sodium polyphosphates. *J. Non. Cryst. Solids* **382**, 11–17 (2013).
23. Toby, B. H. & Von Dreele, R. B. GSAS-II: The genesis of a modern open-source all purpose crystallography software package. *J. Appl. Crystallogr.* **46**, 544–549 (2013).
24. Aden, A. L. & Kerker, M. Scattering of electromagnetic waves from two concentric spheres. *J. Appl. Phys.* **22**, 1242–1246 (1951).
25. Li, R. *et al.* Ionic Potential : A General Material Criterion for the Selection of Highly Efficient Arsenic Adsorbents. *J. Mater. Sci. Technol.* **30**, 949–953 (2014).
26. Jahn, H. A. & Teller, E. Stability of polyatomic molecules in degenerate electronic states—I—Orbital degeneracy. *Proc. R. Soc. London. Ser. A-Mathematical Phys. Sci.* **161**, 220–235 (1937).
27. Rák, Z., Maria, J. & Brenner, D. W. Evidence for Jahn-Teller compression in the ( Mg , Co , Ni , Cu , Zn ) O entropy-stabilized oxide : A DFT study. *Mater. Lett.* **217**, 300–303

- (2018).
28. Albi, T. & Serrano, A. Inorganic polyphosphate in the microbial world. Emerging roles for a multifaceted biopolymer. *World J. Microbiol. Biotechnol.* **32**, 27 (2016).
  29. Huang, R., Wan, B., Hultz, M., Diaz, J. M. & Tang, Y. Phosphatase-Mediated Hydrolysis of Linear Polyphosphates. *Environ. Sci. Technol.* **52**, 1183–1190 (2018).
  30. Holtz, K. M. & Kantrowitz, E. R. The mechanism of the alkaline phosphatase reaction: Insights from NMR, crystallography and site-specific mutagenesis. *FEBS Lett.* **462**, 7–11 (1999).
  31. Schenk, G. *et al.* Crystal structures of a purple acid phosphatase, representing different steps of this enzyme's catalytic cycle. *BMC Struct. Biol.* **8**, 1–13 (2008).
  32. Schenk, G., Mitić, N. Š., Hanson, G. R. & Comba, P. Purple acid phosphatase: A journey into the function and mechanism of a colorful enzyme. *Coord. Chem. Rev.* **257**, 473–482 (2013).
  33. Wan, B., Huang, R., Diaz, J. M. & Tang, Y. Polyphosphate adsorption and hydrolysis on aluminum oxides. *Environ. Sci. Technol.* **53**, 9542–9552 (2019).
  34. Christ, J. J., Willbold, S. & Blank, L. M. Methods for the Analysis of Polyphosphate in the Life Sciences. *Anal. Chem.* **92**, 4167–4176 (2020).
  35. Mandala, V. S. *et al.* Bacterial phosphate granules contain cyclic polyphosphates: Evidence from <sup>31</sup>P solid-state NMR. *J. Am. Chem. Soc.* **142**, 18407–18421 (2020).
  36. Nielsen, P. H. *et al.* A conceptual ecosystem model of microbial communities in enhanced biological phosphorus removal plants. *Water Res.* **44**, 5070–5088 (2010).
  37. Herbst, F. A., Dueholm, M. S., Wimmer, R. & Nielsen, P. H. The Proteome of *Tetrasphaera elongata* is adapted to Changing Conditions in Wastewater Treatment Plants.

- Proteomes* **7**, (2019).
38. Hupfer, M., Gtichter, R. & Ruegger, R. R. Polyphosphate in lake sediments: <sup>31</sup>P NMR spectroscopy as a tool for its identification. *Limnol. Oceanogr.* **40**, 610–617 (1995).
  39. Thakor, N., Trivedi, U. & Patel, K. C. Microbiological and biotechnological aspects of biodegradable plastics: Poly(hydroxyalkanoates). *Indian J. Biotechnol.* **5**, 137–147 (2006).
  40. Zakaria, M. R., Ariffin, H., Abd-Aziz, S., Hassan, M. A. & Shirai, Y. Improved Properties of Poly(3-hydroxybutyrate- co -3-hydroxyvalerate) Produced by Comamonas sp. EB172 Utilizing Volatile Fatty Acids by Regulating the Nitrogen Source. *Biomed Res. Int.* **2013**, (2013).
  41. Albuquerque, P. B. S. & Malafaia, C. B. Perspectives on the production, structural characteristics and potential applications of bioplastics derived from polyhydroxyalkanoates. *Int. J. Biol. Macromol.* **107**, 615–625 (2018).
  42. Kansiz, K., Billman-Jacobe, H. & McNaughton, D. Quantitative determination of the biodegradable polymer poly( $\beta$ -hydroxybutyrate) in a recombinant Escherichia coli strain by use of mid-infrared spectroscopy and multivariate statistics. *Appl. Environ. Microbiol.* **66**, 3415–3420 (2000).
  43. Anderson, A. J. & Dawes, E. A. Occurrence, metabolism, metabolic role, and industrial uses of bacterial polyhydroxyalkanoates. *Microbiol. Rev.* **54**, 450–472 (1990).
  44. Witholt, B. & Kessler, B. Perspectives of medium chain length poly (hydroxyalkanoates), a versatile set of bacterial bioplastics. *Curr. Opin. Biotechnol.* **10**, 279–285 (1999).
  45. Weiss, M. *et al.* Permanent draft genome sequence of Comamonas testosteroni KF-1. *Stand. Genomic Sci.* **8**, 239–254 (2013).
  46. Wu, Y., Zaiden, N. & Cao, B. The core- and pan-genomic analyses of the genus

- Comamonas: From environmental adaptation to potential virulence. *Front. Microbiol.* **9**, 1–12 (2018).
47. Liu, L. *et al.* High correlation between genotypes and phenotypes of environmental bacteria *Comamonas testosteroni* strains. *BMC Genomics* **16**, 1–14 (2015).
  48. Aristilde, L. *et al.* Glyphosate-Induced Specific and Widespread Perturbations in the Metabolome of Soil *Pseudomonas* Species. *Front. Environ. Sci.* **5**, (2017).
  49. Wilkes, R. A., Mendonca, C. M. & Aristilde, L. A cyclic metabolic network in *Pseudomonas protegens* Pf-5 prioritizes the Entner-Doudoroff pathway and exhibits substrate hierarchy during carbohydrate coutilization. *Appl. Environ. Microbiol.* **85**, 1–19 (2019).
  50. Sasnow, S. S., Wei, H. & Aristilde, L. Bypasses in intracellular glucose metabolism in iron-limited *Pseudomonas putida*. *Microbiologyopen* **5**, 3–20 (2016).
  51. Clasquin, M. F., Melamud, E. & Rabinowitz, J. D. LC-MS data processing with MAVEN: A metabolomic analysis and visualization engine. *Curr. Protoc. Bioinforma.* 1–23 (2012) doi:10.1002/0471250953.bi1411s37.
  52. Millard, P. *et al.* IsoCor: Isotope correction for high-resolution MS labeling experiments. *Bioinformatics* **35**, 4484–4487 (2019).
  53. Padovani, G., Emiliani, G., Giovanelli, A., Traversi, M. L. & Carlozzi, P. Assessment of glycerol usage by five different purple non-sulfur bacterial strains for bioplastic production. *J. Environ. Chem. Eng.* **6**, 616–622 (2018).
  54. Brown, M. R. *et al.* Biochemical composition of new yeasts and bacteria evaluated as food for bivalve aquaculture. *Aquaculture* **143**, 341–360 (1996).
  55. Yap, L. F., Lee, Y. K. & Poh, C. L. Mechanism for phenol tolerance in phenol-degrading

- Comamonas testosteroni strain. *Appl. Microbiol. Biotechnol.* **51**, 833–840 (1999).
56. Caspi, R. *et al.* The MetaCyc database of metabolic pathways and enzymes and the BioCyc collection of pathway/genome databases. *Nucleic Acids Res.* **40**, 742–753 (2012).
57. Shupletsov, M. S. *et al.* OpenFLUX2: 13 C-MFA modeling software package adjusted for the comprehensive analysis of single and parallel labeling experiments. *Microb. Cell Fact.* **13**, 1–25 (2014).
58. Waldbauer, J., Zhang, L., Rizzo, A. & Muratore, D. DiDO-IPTL: A Peptide-Labeling Strategy for Precision Quantitative Proteomics. *Anal. Chem.* **89**, 11498–11504 (2017).
59. Saldanha, A. J. Java Treeview - Extensible visualization of microarray data. *Bioinformatics* **20**, 3246–3248 (2004).
60. Pinhal, S., Ropers, D., Geiselman, J. & De Jong, H. Acetate metabolism and the inhibition of bacterial growth by acetate. *J. Bacteriol.* **201**, 1–19 (2019).
61. Willems, A. & De Vos, P. Comamonas. in *The Prokaryotes: a handbook on the biology of bacteria. Vol. 5* 723–736 (Springer, 2006).
62. van Duuren, J. B. J. H. *et al.* Reconciling in vivo and in silico key biological parameters of Pseudomonas putida KT2440 during growth on glucose under carbon-limited condition. *BMC Biotechnol.* **13**, (2013).
63. Ahn, S., Jung, J., Jang, I. A., Madsen, E. L. & Park, W. Role of glyoxylate shunt in oxidative stress response. *J. Biol. Chem.* **291**, 11928–11938 (2016).
64. Geisseler, D., Horwath, W. R., Joergensen, R. G. & Ludwig, B. Pathways of nitrogen utilization by soil microorganisms - A review. *Soil Biol. Biochem.* **42**, 2058–2067 (2010).
65. Wanner, B. L. Phosphorus Assimilation and Control of the Phosphate Regulon. *Escherichia coli Salmonella Cell. Mol. Biol.* **1**, 1357–1381 (1996).

66. Santos-beneit, F. The Pho regulon : a huge regulatory network in bacteria. *Front. Microbiol.* **6**, 1–13 (2015).

## APPENDIX A: Chapter 1

**Table S1.1** Comparison of essential bond lengths (Å) and angles (°) within the Ca-pyrophosphate structure from the simulation (average  $\pm$  standard deviation) and the reference (Gras *et al.* 2016). Atom numbered according to the reference.

Bond length	Simulation	Reference	% difference	Bond angle	Simulation	Reference	% difference
O1 - P9	1.593 $\pm$ 0.040	1.492	6.8	O1-P9-O3	101.8 $\pm$ 4.0	113.4	10.2
O8 - P10	1.580 $\pm$ 0.036	1.581	0.0	O1-P9-O4	111.2 $\pm$ 7.6	112.7	1.4
O8 - P9	1.612 $\pm$ 0.045	1.688	4.5	O1-P9-O8	115.9 $\pm$ 3.4	107.0	8.3
O7 - P10	1.517 $\pm$ 0.037	1.525	0.5	O4-P9-O8	113.3 $\pm$ 9.0	116.4	2.7
O3 - P9	1.480 $\pm$ 0.028	1.510	2.0	O3-P9-O4	100.2 $\pm$ 4.6	104.2	3.8
O4 - P9	1.635 $\pm$ 0.041	1.551	5.4	O3-P9-O8	112.1 $\pm$ 5.4	101.5	10.5
O5 - P10	1.581 $\pm$ 0.039	1.533	3.1	P9-O8-P10	97.2 $\pm$ 3.6	128.3	24.2
O6 - P10	1.477 $\pm$ 0.029	1.501	1.6	O5-P10-O7	94.6 $\pm$ 5.6	113.3	16.5
Ca11 - O1	2.585 $\pm$ 0.074	2.372	9.0	O5-P10-O6	109.0 $\pm$ 4.9	106.2	2.7
O5 - Ca2	2.772 $\pm$ 0.086	2.343	18.3	O5-P10-O8	107.3 $\pm$ 7.1	106.0	1.2
				O6-P10-O7	50.4 $\pm$ 8.1	114.7	56.1
				O7-P10-O8	100.1 $\pm$ 12.0	106.4	5.9
				O6-P10-O8	116.8 $\pm$ 24.0	109.9	6.2

**Table S1.2** Coordination distance (average  $\pm$  standard deviation, Å) and number (CN) of the metal (M)-polyphosphate (polyP) complexes. The reported values have been recalculated based on the values reported in Table 1.1. Instead of calculating the distance and CN up to the global minimum as in Table 1.1, the values here are recalculated up to the radial distance at which the CN value was closest to the rounded up whole number of the CN values reported in Table 1.1.

M (metal)	M-ligand O		M-bridging O		M-water O	
	Distance	CN	Distance	CN	Distance	CN
<i>M-polyP-10 complexes</i>						
Na <sup>+</sup>	2.58 $\pm$ 0.56	2.07	2.73 $\pm$ 0.55	1.01	2.73 $\pm$ 0.51	3.07
K <sup>+</sup>	2.70 $\pm$ 0.46	1.99	2.88 $\pm$ 0.49	1.01	2.76 $\pm$ 0.35	2.06
Ca <sup>2+</sup>	2.43 $\pm$ 0.37	1.96	3.09 $\pm$ 0.75	2.03	2.40 $\pm$ 0.25	0.97
Mg <sup>2+</sup>	1.98 $\pm$ 0.32	2.01	2.64 $\pm$ 0.70	2.04	2.52 $\pm$ 0.42	0.96
<i>M-polyP-30 complexes</i>						
Na <sup>+</sup>	2.79 $\pm$ 0.68	3.00	2.85 $\pm$ 0.65	1.03	2.46 $\pm$ 0.35	1.97
K <sup>+</sup>	2.76 $\pm$ 0.49	1.99	3.24 $\pm$ 0.60	0.96	2.67 $\pm$ 0.34	1.94
Ca <sup>2+</sup>	2.52 $\pm$ 0.46	1.98	2.97 $\pm$ 0.51	1.00	2.25 $\pm$ 0.20	0.97
Mg <sup>2+</sup>	2.43 $\pm$ 0.58	2.98	2.46 $\pm$ 0.53	1.02	2.46 $\pm$ 0.46	1.98

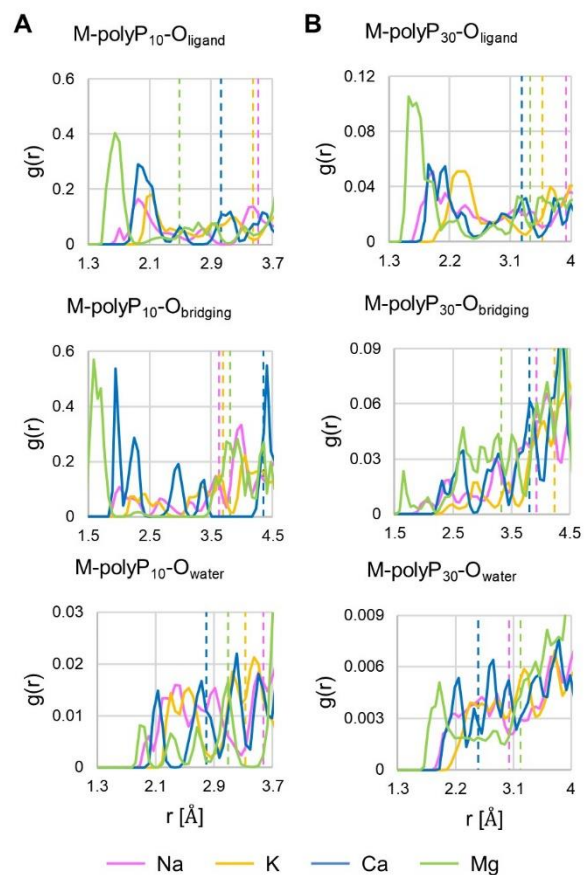


**Figure S1.1** Radial distribution functions (RDF,  $g(r)$ ) of different O groups within the metal (M)-polyphosphate (polyP) complexes: (A) polyP-10 and (B) polyP-30. The dotted lines mark the radial distance at which the calculated coordination number (CN) was closest to the rounded up whole number. Color code: Na (pink), K (yellow), Ca (blue), and Mg (green).

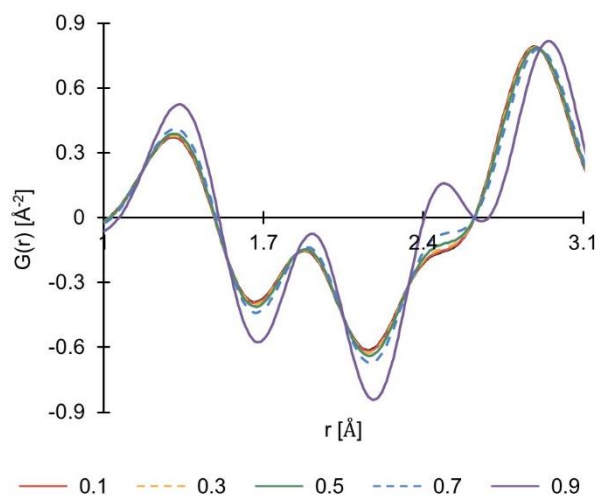


**Figure S1.2** Pair distribution function (PDF,  $G(r)$ ) obtained from total X-ray scattering, both without (black) and with various reference solution correction factors (0.1, 0.3, 0.5, 0.7, and 0.9).

**Details of the pair distribution function (PDF) calculation.** The experiments were straightforward X-ray powder diffraction measurements. From the coherent part,  $I^{coh}(Q)$ , of the measured total diffracted intensity of the material we find the total scattering structure function,  $S(Q)$

$$S(Q) = \frac{I^{coh}(Q) - \sum c_i |f_i(Q)|^2}{|\sum c_i f_i(Q)|^2} + 1 \quad (1)$$

where the coherent intensity is corrected for background and other experimental effects and normalized by the flux and number of atoms in the sample. Here,  $c_i$  and  $f_i$  are the atomic concentration and X-ray atomic form factor, respectively, for the atomic species of type  $i$ . Momentum transfer,  $Q$ , is given by

$$Q = 4\pi \sin \theta / \lambda \quad (2)$$

By Fourier transforming the expression  $Q[S(Q) - 1]$  we have

$$G(r) = (2/\pi) \int_{Q=0}^{Q_{\max}} Q[S(Q) - 1] \sin(Q \cdot r) dQ \quad (3)$$

where  $G(r)$  is the atomic pair distribution function which is also defined as

$$G(r) = 4\pi \cdot r [\rho(r) - \rho_0] \quad (4)$$

where  $\rho_0$  is the average atomic number density,  $\rho(r)$  is the atomic pair-density and  $r$  is a radial distance. The function  $G(r)$  gives information about the number of atoms in a spherical shell of unit thickness at a distance  $r$  from a reference atom. Finally, the experimental  $G(r)$  can be compared and refined against a theoretical  $G(r)$  from a structural model given by

$$G(r) + 4\pi \cdot r \cdot \rho_0 = \frac{1}{r} \sum_{\nu} \sum_{\mu} \frac{f^{(0)}_{\nu} f^{(0)}_{\mu}}{\langle f^{(0)} \rangle^2} \delta(r - r_{\nu\mu}) \quad (5)$$

In theory,  $Q_{max}$  from equation (3) should be infinite but experimentally is always a finite number. In order to have good resolution, values of  $Q > 20 \text{ \AA}^{-1}$  are desirable therefore short wavelengths are necessary according to equation (2).

Unlike a conventional X-ray or neutron powder diffraction experiment, the PDF analysis treats both the Bragg and diffuse scattering on an equal basis. Because the data analysis does not presume any periodicity, the technique is very useful for examining samples if distortions found in a specific single crystal are representative of the total bulk of the sample.

## APPENDIX B: Chapter 2

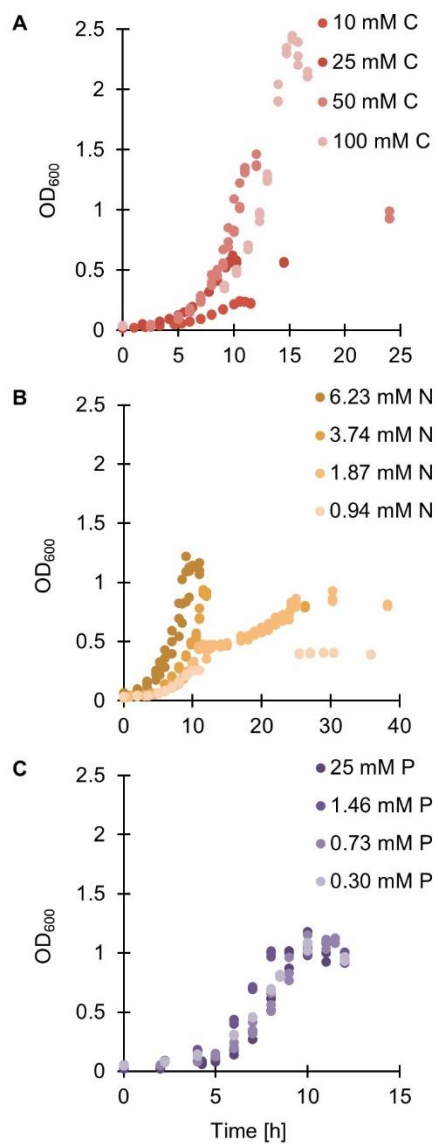


**Figure S2.1** Growth curves for *C. testosteroni* KF-1 fed on acetate as a sole carbon source with varying nutrient concentrations: (A) different acetate concentrations, (B) different NH<sub>4</sub>Cl concentrations, and (C) different total PO<sub>4</sub> concentrations. The data for independent biological replicates ( $n = 3$  or  $6$ ) were compiled for each nutrient concentration.

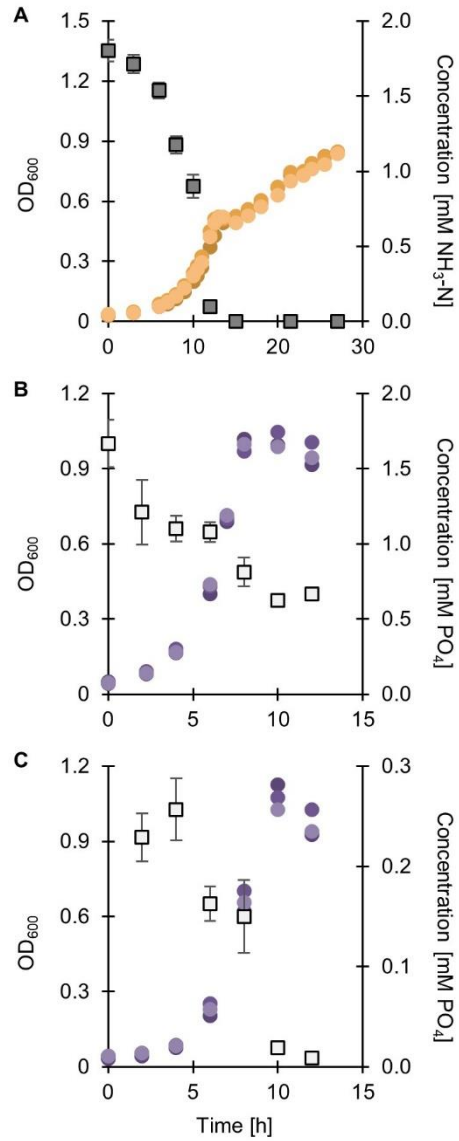


**Figure S2.2** Kinetic profile of extracellular N or P (square) overlaid with the OD<sub>600</sub> (circle): NH<sub>3</sub>-N was monitored for the N-dependent condition (A), and PO<sub>4</sub> was monitored for the P-dependent conditions 1 and 2 (B and C). N and P concentration data are shown as mean  $\pm$  standard deviation for biological replicates ( $n = 3$  or  $6$ ).

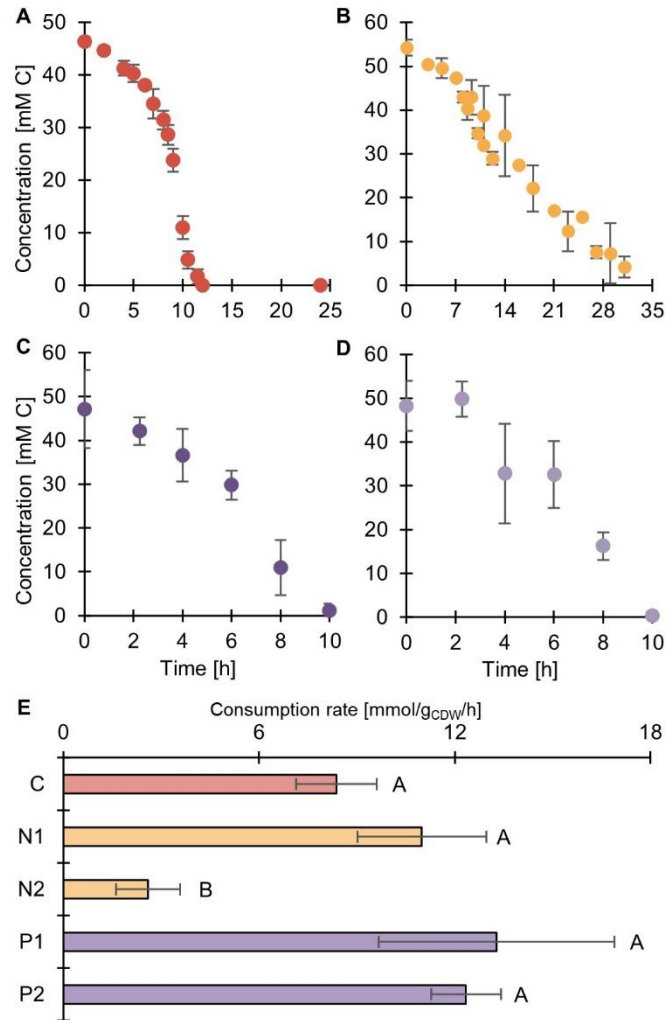


**Figure S2.3** Acetate consumption measured with <sup>1</sup>H-NMR for the following conditions: (A) control (C), (B) N-dependent condition, (C) P-dependent condition 1 (P1), and (D) P-dependent condition 2 (P2). (E) Acetate consumption rate [mmol·g<sub>CDW</sub><sup>-1</sup>·h<sup>-1</sup>] was calculated for each condition with the N-dependent condition divided into the first (N1) and second (N2) growth phase. Significant differences ( $p < 0.05$ ) are denoted by changes in letters. Data are shown as mean  $\pm$  standard deviation for biological replicates ( $n = 3$ ).

**Figure S2.4** Metabolite  $^{13}\text{C}$ -labeling patterns at two different time points (TP) during exponential growth on  $[\text{U-}^{13}\text{C}]$ -acetate for (A) control ( $\text{OD}_{600} \sim 0.35$  and  $0.7$ ) (B) N1 ( $\text{OD}_{600} \sim 0.17$  and  $0.3$ ), and (C) N2 ( $\text{OD}_{600} \sim 0.6$  and  $0.7$ ) conditions. Vertical axes represent the fraction of each labeling pattern.

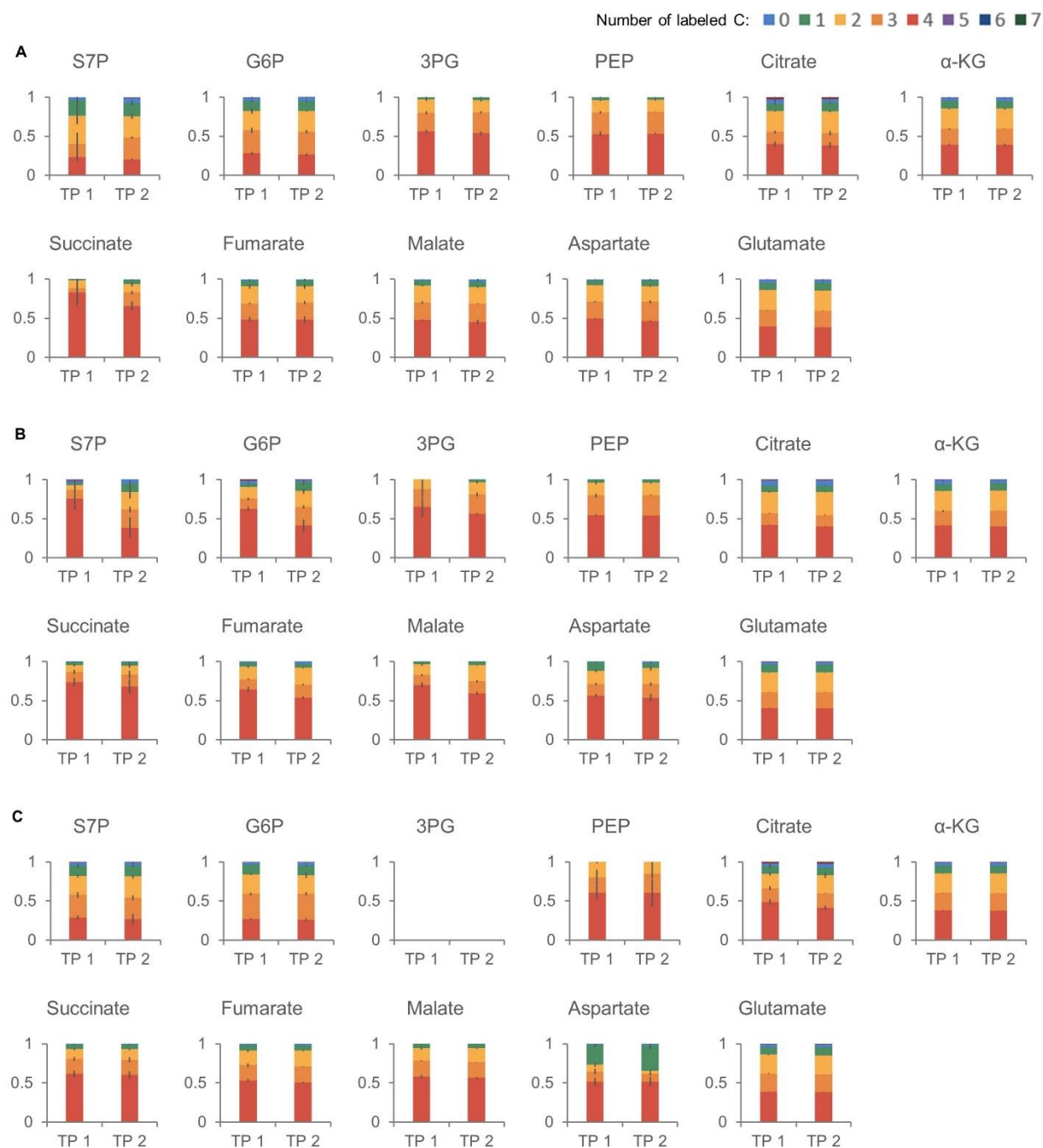


**Table S2.1** Metabolic rates determined by the MFA of [U-<sup>13</sup>C]-acetate by *C. testosteroni* KF-1 using the OpenFLUX2 software. Listed values are normalized to 100% acetate consumption respective to each condition. Absolute fluxes [mmol·g<sub>CDW</sub><sup>-1</sup>·h<sup>-1</sup>] are illustrated in Figure 2.2.

Reactions	Control	N1	N2
ACE_EX => ACCOA	100.3 ± 0.2	98.9 ± 0.5	98.6 ± 3.0
SUCC => 0.5 FUM + 0.5 FUM	43.6 ± 5.4	50.6 ± 2.5	59.6 ± 11.9
FUM => MAL	43.6 ± 5.4	50.6 ± 2.5	59.6 ± 11.9
MAL => OAA	131.6 ± 11.9	75.8 ± 11.0	103.9 ± 8.1
ACCOA + OAA => CIT	46.8 ± 5.2	52.9 ± 2.8	70.7 ± 9.1
CIT => AKG + CO2	16.6 ± 7.5	36.6 ± 1.5	11.3 ± 5.3
AKG => 0.5 SUCC + 0.5 SUCC + CO2	13.4 ± 7.7	34.3 ± 2.0	0.2 ± 4.9
CIT => 0.5 SUCC + 0.5 SUCC + GLOX	30.2 ± 2.4	16.3 ± 1.7	59.4 ± 8.9
GLOX + ACCOA => MAL	30.2 ± 2.4	16.3 ± 1.7	59.4 ± 8.9
OAA => PEP + CO2	44.3 ± 10.7	10.6 ± 9.6	31.8 ± 15.4
OAA => PYR + CO2	36.2 ± 24.9	9.9 ± 4.1	0.6 ± 27.4
MAL => PYR + CO2	-57.9 ± 14.1	-8.9 ± 12.9	15.0 ± 28.3
PYR => ACCOA + CO2	0.0 ± 0.0	-4.8 ± 1.8	41.4 ± 12.0
PYR => PEP	-28.6 ± 11.6	0.4 ± 10.1	-27.9 ± 16.3
PEP => 3PG	12.1 ± 0.6	8.0 ± 1.3	2.8 ± 0.7
3PG => GAP	7.9 ± 0.3	5.3 ± 1.0	2.0 ± 0.5
GAP => DHAP	3.3 ± 0.1	2.2 ± 0.5	0.8 ± 0.2
DHAP + GAP => FBP	2.8 ± 0.1	1.9 ± 0.3	0.7 ± 0.2
FBP => F6P	2.8 ± 0.1	1.9 ± 0.3	0.7 ± 0.2
F6P => G6P	1.0 ± 0.0	0.5 ± 0.1	0.2 ± 0.1
E4P + F6P => S7P + GAP	0.1 ± 0.0	0.2 ± 0.1	0.0 ± 0.2
S7P + GAP => R5P + Xu5P	0.1 ± 0.0	0.2 ± 0.1	0.0 ± 0.2
F6P + GAP => E4P + Xu5P	1.7 ± 0.1	1.2 ± 0.2	0.5 ± 0.3
Xu5P => R5P	1.8 ± 0.1	1.4 ± 0.3	0.5 ± 0.3
ACCOA = PHB	6.2 ± 0.7	10.0 ± 3.8	7.1 ± 12.3

**Table S2.2** Biomass efflux and metabolite secretion rates were determined by the MFA of [U-<sup>13</sup>C]-acetate by *C. testosteroni* KF-1 using the OpenFLUX2 software. Listed values are normalized to 100% acetate consumption respective to each condition. Absolute fluxes [mmol·g<sub>CDW</sub><sup>-1</sup>·h<sup>-1</sup>] are illustrated in Figure 2.2.

Reactions	Control	N1	N2
3PG => Biomass	4.2 ± 0.3	2.7 ± 1.1	0.9 ± 0.8
AKG => Biomass	3.2 ± 0.2	2.3 ± 1.2	0.3 ± 0.5
DHAP => Biomass	0.5 ± 0.0	0.3 ± 0.1	0.1 ± 0.0
E4P => Biomass	1.7 ± 0.1	1.0 ± 0.3	0.4 ± 0.4
G6P => Biomass	1.0 ± 0.0	0.5 ± 0.1	0.2 ± 0.1
OAA => Biomass	4.4 ± 0.3	2.3 ± 1.5	0.8 ± 0.6
PEP => Biomass	3.6 ± 0.2	3.1 ± 1.1	1.1 ± 0.3
PYR => Biomass	6.9 ± 1.0	5.4 ± 0.7	1.7 ± 1.1
R5P => Biomass	1.9 ± 0.1	1.5 ± 0.4	0.6 ± 0.4
ACCOA => Biomass	17.2 ± 1.9	14.9 ± 1.8	2.9 ± 2.5
PYR <sub>in</sub> => PYR <sub>ex</sub>	-	-	0.5 ± 0.4
AKG <sub>in</sub> => AKG <sub>ex</sub>	-	-	10.8 ± 3.3

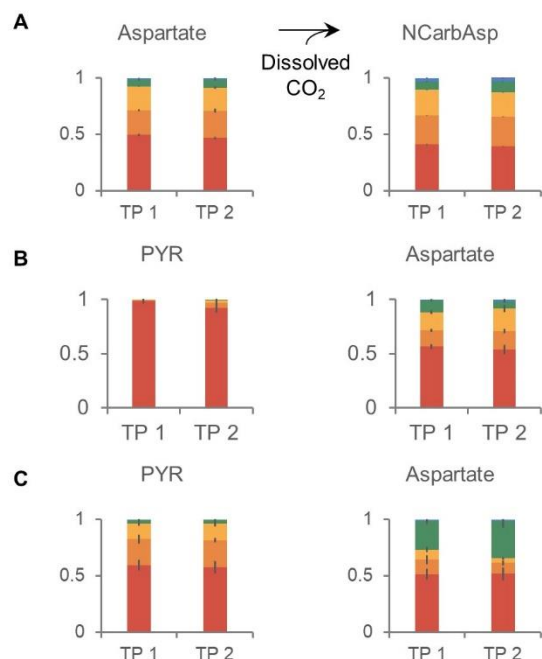


**Figure S2.5** Estimation of CO<sub>2</sub> labeling from the biosynthesis of (A) N-carbamoyl-aspartate (NCarbAsp) from aspartate for the control condition, (B) aspartate from PYR for N1 and (C) N2. NCarbAsp and aspartate are formed from aspartate and pyruvate, respectively, with the incorporation of dissolved CO<sub>2</sub>. The addition of <sup>13</sup>C-labeled carbon in NCarbAsp and Asp is considered an addition of labeled dissolved CO<sub>2</sub>. Color schemes equal to that for Figure S2.4. Vertical axes represent the fraction labeling patterns for each metabolite.